JAMES | Journal of Advances in Modeling Earth Systems®

RESEARCH ARTICLE
10.1029/2025MS005420

Special Collection:
EMIT: The Earth Surface Mineral Dust Science Investigation

Modeling Large Dust Aerosols in the Community Earth System Model Version 2 (CESM2)

Longlei Li[1], Natalie M. Mahowald[1], Xiaohong Liu[2], María Gonçalves Ageitos[3,4], Ziming Ke[5], Danny M. Leung[6], Carlos Pérez García-Pando[3,7], Ron L. Miller[8], Vincenzo Obiso[3], Paul Ginoux[9], Jasper F. Kok[10], Paola Formenti[11], Claudia Di Biagio[11], Philip G. Brodrick[12], David R. Thompson[12], Roger N. Clark[13], Gregory S. Okin[14], Robert O. Green[12], Bo Zhou[14], Samuel Albani[15], and Adeyemi A. Adebiyi[16]

[1]Department of Earth and Atmospheric Sciences, Cornell University, Ithaca, NY, USA, [2]Department of Atmospheric Sciences, Texas A&M University, College Station, TX, USA, [3]Barcelona Supercomputing Center, Barcelona, Spain, [4]Department of Project and Construction Engineering, Universitat Politècnica de Catalunya–Barcelona Tech, Terrassa, Spain, [5]Lawrence Livermore National Laboratories, Livermore, CA, USA, [6]Atmospheric Chemistry Observations and Modeling Laboratory, NSF National Center for Atmospheric Research, Boulder, CO, USA, [7]ICREA, Catalan Institution for Research and Advances Studies, Barcelona, Spain, [8]NASA Goddard Institute for Space Studies, New York, NY, USA, [9]NOAA Geophysical Fluid Dynamics Laboratory, Princeton, NJ, USA, [10]Department of Atmospheric and Oceanic Sciences, University of California, Los Angeles, Los Angeles, CA, USA, [11]Université Paris Cité and Université Paris Est Creteil, CNRS, LISA, Paris, France, [12]Jet Propulsion Laboratory, California Institute of Technology, Pasadena, CA, USA, [13]Planetary Science Institute, Tucson, AZ, USA, [14]Department of Geography, University of California, Los Angeles, Los Angeles, CA, USA, [15]Department of Environmental and Earth Sciences, University of Milano-Bicocca, Milan, Italy, [16]Department of Life and Environmental Sciences, University of California Merced, Merced, CA, USA

Abstract Dust aerosols have a wide size distribution from less than 0.1 to over 100 μm and dominate Earth's atmospheric aerosol mass. However, most Earth system models (ESMs) inadequately represent dust aerosols larger than 10 μm in diameter, limiting the accuracy of the simulated dust cycle and climate impacts. Here, we introduce a new modeling framework that captures the full observed size distribution of dust aerosols, incorporating recent advances into a mineral-resolved version of the Community ESM, while addressing known issues in previous versions. Comprehensive evaluation against diverse observations of bulk dust and component minerals demonstrates that the model reproduces the observed dust cycle across particle sizes. Incorporating the previously unrepresented large-dust fractions substantially alters dust budget estimates, highlighting potential changes in simulated climate impacts and underscoring the importance of comprehensive size-resolved dust modeling. Despite these advancements, uncertainties persist. Our results indicate that a size-dependent reduction in settling velocity is required to reproduce the observed dust size distribution downwind of source regions. Specifically, in the new model, the gravitational settling velocity of dust particles larger than 10 μm in diameter must be reduced by as much as 85% to achieve agreement with observations. This empirical reduction serves as a constraint on physics-based models of dust settling. Future developments should address misrepresented physical processes that hinder accurate modeling of the large dust aerosol transport. Expanding observational data sets covering the full-size distribution is also essential to better constrain the dust cycle and improve the representation of dust optical properties and climate effects.

Plain Language Summary Mineral dust constitutes the largest mass of airborne particles on Earth. These particles span a wide range of sizes from tiny to giant, but not all sizes play an equally important role. As particles that both scatter and absorb solar and thermal radiation while delivering vital nutrients to ecosystems, mineral dust plays a critical role in various Earth system processes and in projections of future climate changes. However, most Earth system models (ESMs), including the Community ESM version 2 (CESM2), either neglect or underrepresent particles large than 10 microns in diameter, limiting our understanding of dust's full influence on climate. Furthermore, the CESM2 dust module, including its mineral-resolved version used in this study, lacks several key physical processes known to affect dust emission and transport. This study enhances the representation of dust aerosols in the mineral-resolved version of CESM2 by extending the upper size limit of simulated dust particles to 70 microns at emission and adding omitted physical processes for dust emission based on the latest scientific findings. The updated model is evaluated against a wide range of observations under present-day climate conditions.

Key Points:

- A new model is developed to simulate dust aerosols for a wide distribution of sizes with observational constraints and improved mineralogy
- Including particles larger than 10 microns in diameter greatly alters simulated dust budgets while not degrading finer dust representation
- Challenges remain, especially for representing the physical mechanisms that transport super-coarse and giant dust in Earth system models

Supporting Information:

Supporting Information may be found in the online version of this article.

Correspondence to:

L. Li,
ll859@cornell.edu

Citation:

Li, L., Mahowald, N. M., Liu, X., Gonçalves Ageitos, M., Ke, Z., Leung, D. M., et al. (2026). Modeling large dust aerosols in the Community Earth System Model Version 2 (CESM2). *Journal of Advances in Modeling Earth Systems*, *18*, e2025MS005420. https://doi.org/10.1029/2025MS005420

Received 14 AUG 2025
Accepted 13 FEB 2026

Author Contributions:

Conceptualization: Longlei Li
Data curation: Longlei Li, Natalie M. Mahowald, María Gonçalves Ageitos, Carlos Pérez García-Pando, Ron L. Miller, Vincenzo Obiso, Paul Ginoux, Philip G. Brodrick, David R. Thompson, Roger

N. Clark, Gregory S. Okin, Robert O. Green, Bo Zhou, Samuel Albani
Formal analysis: Longlei Li
Funding acquisition: Natalie M. Mahowald
Investigation: Longlei Li
Methodology: Longlei Li
Resources: Natalie M. Mahowald, Xiaohong Liu, María Gonçalves Ageitos, Ziming Ke, Carlos Pérez García-Pando, Ron L. Miller, Vincenzo Obiso, Paul Ginoux, Jasper F. Kok, Paola Formenti, Claudia Di Biagio, Philip G. Brodrick, David R. Thompson, Roger N. Clark, Gregory S. Okin, Robert O. Green, Bo Zhou, Samuel Albani, Adeyemi A. Adebiyi
Software: Longlei Li, Xiaohong Liu, Ziming Ke, Danny M. Leung, Jasper F. Kok
Validation: Longlei Li
Visualization: Longlei Li
Writing – original draft: Longlei Li
Writing – review & editing: Longlei Li, Natalie M. Mahowald, Xiaohong Liu, María Gonçalves Ageitos, Ziming Ke, Danny M. Leung, Carlos Pérez García-Pando, Ron L. Miller, Vincenzo Obiso, Paul Ginoux, Jasper F. Kok, Paola Formenti, Claudia Di Biagio, Philip G. Brodrick, David R. Thompson, Roger N. Clark, Gregory S. Okin, Robert O. Green, Bo Zhou, Samuel Albani, Adeyemi A. Adebiyi

1. Introduction

Mineral dust, the most abundant aerosol by mass (Gliß et al., 2021), has diverse climate impacts (Kok et al., 2023) through direct interactions with radiation, indirectly modifying cloud properties, and by depositing micronutrients (e.g., iron) and macronutrients (e.g., phosphorus) to marine and terrestrial ecosystems (Jickells et al., 2005; Mahowald, 2011; Mahowald et al., 2010, 2018; Mccutcheon et al., 2021; Meskhidze et al., 2005). Dust influences weather and climate, especially near source regions, and acts as an air pollutant causing transportation hazards (Bhattachan et al., 2019) and impacting human health (Goudie, 2014; Maki et al., 2022; Pérez García-Pando et al., 2014). Accurately quantifying these impacts at large (e.g., continental and global) scales requires models capable of reproducing the spatiotemporal life cycle and physicochemical properties of dust aerosols, which are sensitive to dust size (Mahowald et al., 2014). Such capability, however, remains highly limited, partially due to a lack of high-quality observations (Mahowald, Li, Albani, et al., 2024) with sufficient coverage to constrain key factors, such as dust size (Baker & Jickells, 2006; Liao & Seinfeld, 1998) and mineral composition (Perlwitz et al., 2015b; Sokolik & Toon, 1999), which remain especially uncertain (Adebiyi & Kok, 2020; Li et al., 2021; Mahowald et al., 2014).

Dust aerosols, typically represented by multiple modes or bins characterized by particle size in Earth system models (ESMs), have a broad diameter range from just above 0.1 to hundreds of microns (Adebiyi et al., 2023). Like many other ESMs, various versions of the Community ESM (CESM) have focused on simulating dust particles smaller than 10 μm in geometric diameter (herein referred to as "diameter" unless stated otherwise and often subdivided into three categories: fine, smaller than 1.0 μm; fine/coarse, 1.0–5.0 μm; and medium coarse, 5.0–10 μm) (Zender, Newman, & Torres, 2003), even though dust particles between 10 and 20 μm (super coarse), and even larger than 20 μm (super coarse/giant), have been observed during transport from North Africa to Barbados (Prospero et al., 1970) or East Asia to the North Pacific (Betzer et al., 1988). Particles larger than 10 μm in diameter, especially those larger than 20 μm, were assumed to be rare and received less attention, because (a) most were thought to be rapidly removed from the atmosphere due to gravitational settling and because they are also more likely to be removed through below-cloud scavenging (Jones et al., 2022) because of their larger cross-sectional area presented to falling precipitation; (b) they were considered less relevant to climate in part due to smaller extinction at visible wavelengths per unit pass (Mahowald et al., 2014); (c) conventional dry-deposition mechanisms (Petroff & Zhang, 2010; Zender, Newman, & Torres, 2003; L. Zhang et al., 2001) underestimate their lifetimes and long-range transport (Drakaki et al., 2022; Ginoux, 2003; Ratcliffe et al., 2024); and (d) air quality measurements typically focus on dust particles with aerodynamic diameters smaller than 2.5 μm (Particular Matter: $PM_{2.5}$) and 10 μm (PM_{10}) (Mahowald et al., 2025).

The assumption of a 10 μm cutoff diameter in the dust size distribution was recognized as insufficient for dust aerosol modeling in a limited number of early studies over two decades ago (Betzer et al., 1988; Mahowald et al., 2005). Such limitations gained more attention following recent campaign measurements using in situ and remote sensing instruments (Ryder et al., 2013, 2018, 2019; van der Does et al., 2016; Weinzierl et al., 2009, 2017). These measurements indicate that dust aerosols with diameters larger than 10 μm and up to 40 μm are observed up to 2,000 km downwind of North Africa (van der Does et al., 2018). A synthesis of model and observational data also highlights that dust particles in the 10–20 μm diameter range greatly contribute to regional deposition in areas such as the Southern Ocean (Adebiyi et al., 2023).

Most current ESMs, including CESM with either the Bulk Aerosol Module (BAM) (Adebiyi & Kok, 2020) or Modal Aerosol Module (MAM) (Li et al., 2022b; X. Liu et al., 2016), underestimate the abundance of dust particles larger than 5.0 μm in diameter (Adebiyi & Kok, 2020), and even more so for particles larger than 10 μm involved in long-range transport (Ratcliffe et al., 2024), compared to observations. This underrepresentation can potentially bias estimates of dust aerosol budgets (e.g., smaller cutoff sizes may result in lower emitted mass fluxes, or attribute too much dust to the fine fraction) and assessments of dust impacts on Earth-climate-human interactions (Kok et al., 2023).

To date, only a few studies have attempted to simulate the full size distribution of dust particles in either regional (Drakaki et al., 2022) or global models (Ginoux, 2003; Ratcliffe et al., 2024; Wang et al., 2024), and even fewer in CESM (Meng et al., 2022), although some other models have a dust cutoff size larger than 10 μm in diameter (Gonçalves Ageitos et al., 2023; Klose et al., 2021; Obiso et al., 2024; Perlwitz et al., 2015a). Most CESM-based dust modeling studies have not adequately included particles larger than 10 μm in diameter (Albani et al., 2014; Li et al., 2022b; Meng et al., 2022). This is because they used older model versions or focused on specific objectives

that addressed only limited aspects of dust cycle modeling. For example, Meng et al. (2022) did not focus on model development of the full dust cycle within CESM (version 1) but more specifically on achieving an emitted size distribution consistent with observed dust fluxes. Consequently, their study did not extend model-observation comparisons to other critical dust properties, such as surface concentrations, optical depth, and deposition, all of which warrant further investigation. Ke et al. (2022) extended the maximum dust diameter to 20 μm but did not account for coarser aerosols, which remain abundant and are observed downwind of North Africa. The size distribution simulated by their model also requires evaluation against observations, which are unfortunately lacking, before a reliable assessment of the contribution of dust particles between 10 and 20 μm in diameter can be made. Thus, there remains a need for the development of a more comprehensive representation of the dust cycle, which adequately incorporates the dynamics of super-coarse and giant dust particles, along with measurements for evaluating such a model.

The primary objective of this study is to advance the mineral-resolved CESM2 (Li et al., 2022b) to comprehensively represent dust aerosols across a wide size range, up to 70 μm in geometric diameter at emission (slightly above the conventional diameter boundary between sand and dust particles at 62.5 μm). To achieve this, we develop a ten-mode MAM (MAM10) and constrain the simulated dust size distribution with observations. We also incorporate recent developments into this more comprehensive framework to simulate the climate impacts of dust aerosols.

Specifically, this study introduces several key developments:

1. The new MAM10: We develop this new aerosol module to include dust particles larger than 20 μm and up to 70 μm in geometric diameter at emission within the mineral-resolved Community Atmosphere Model Version 6 (CAM6) framework (Li et al., 2022b) as an extension to the nine-mode MAM (MAM9) in CAM version 5 (CAM5) (Ke et al., 2022), which lacks mineral speciation. The mixing state of dust aerosols with non-dust aerosols, such as sea salt, has been revised as well. The simulated dust size distribution is constrained by comprehensive measurements along dust plume trajectories including the super-coarse and giant dust fractions (Formenti & Di Biagio, 2024).
2. Improved dust emission scheme: We improve the dust emission scheme in the mineral-resolved CESM2 by adding drag partitioning by non-erodible elements (e.g., rocks and vegetation) and intermittency due to the coarse temporal resolution of the model (i.e., 30 min) relative to the timescale of surface wind oscillations (Leung et al., 2023).
3. Updated soil mineralogy atlas: We incorporate a new atlas from the Earth surface Mineral dust source InvesTigation (EMIT) project (Green et al., 2020) to characterize mineralogy in current and potential future erodible soils. Prior to the EMIT mission, dust source composition was estimated from two highly uncertain global soil atlases based on limited mineral measurements and heavily interpolated over the non-agricultural regions that are the key dust source areas (Claquin et al., 1999; Journet et al., 2014). The new EMIT soil mineral atlas produced the first near-global-scale mineral atlas of dust source regions based upon direct measurements and retrievals. This EMIT data set has been shown to significantly reduce uncertainties in dust mineral composition and, consequently, in the simulated shortwave dust direct radiative effect for both the present day and projections for the late 21st century, relative to simulations using pre-EMIT soil atlases (Li, Mahowald, Miller, et al., 2025).
4. Updated optics for iron oxides: We modify the complex refractive index for iron oxides using observationally constrained values, which have been shown to capture both the laboratory-measured dust aerosol optical properties and their relationship with iron oxide content (Li et al., 2024).

The central objective of this study is not to introduce new physically based and state-of-art parameterizations for all dust-related processes, but to quantify the consequences of explicitly resolving super-coarse and giant dust particles in the mineral-resolved CESM2. In contrast to previous CESM dust frameworks, in which a single coarse mode spans a wide diameter range and size-dependent processes act at a mode-mean particle size, the expanded number of modes relaxes a fundamental structural constraint that limited the simultaneous representation of large-particle removal and smaller-coarse-particle transport. By systematically comparing simulations with different dust size representations, we isolate the role of large particles in shaping the modeling of dust emission, transport, and deposition, which could not be robustly assessed within previous CESM dust frameworks.

Below, we describe the old CESM dust aerosol framework (Section 2) and then describe the structural extensions introduced here through MAM10 (Section 3), with particular emphasis on the explicit representation of

Table 1
Dust Mode Parameters in the Four-Mode Modal Aerosol Module (MAM4)

Dust mode	A2 (Aitken)	A1 (accumulation)	A3 (coarse)
Emitted geometric diameter limits (μm) for mass-to-number flux conversions	0.010–0.10	0.10–1.0	1.0–10
Geometric standard deviation (GSD)	1.6	1.8	1.8
Initialized dry geometric mean diameter (GMD) (μm) for the number distribution	0.026	0.11	2.0
Low and upper bounds for simulated dry GMD (μm; number distribution)	0.0087–0.052	0.054–0.44	1.0–4.0
Emitted mass fraction			
Fractional contribution to total dust	0.0010	0.011	0.99
From clay	1.0	1.0	0.69
From silt	0.0	0.0	0.31

super-coarse and giant dust particles. This paper evaluates the performance of the new mineral-resolved CESM2 in simulating key features of the observed dust cycle, including the contribution of newly incorporated super-coarse and giant dust particles. Our analysis focuses on the updated model, with comparisons made to the previous version (Li et al., 2022b), but without attributing improvements to specific model developments.

2. General Model Overview and Treatments in Previous Versions

We utilize the National Center for Atmospheric Research (NCAR) CESM version 2.1.0 (CESM2.1.0). This model comprises multiple components, including the atmosphere component (CAM6) and the land component (Community Land Model version 4.5; CLM4.5), crucial for representing Earth's processes in climate projections.

Parameterizations for eolian processes responsible for dust emission are primarily implemented in CLM4.5, which communicates with CAM6 through a coupler, transmitting vertical emission fluxes. The total vertical dust emission flux is computed using the same emission physics for all particle sizes, and no size-specific emission mechanisms are applied in all the models used here. CAM6 then redistributes the emission flux into different aerosol modes when employing a MAM, and simulates the transport, deposition, and climate impacts of dust aerosols. Dust aerosol transport and deposition in CAM6 employs identical numerical formulations across all particle sizes, with no size-specific physical mechanisms applied in all the models used here as well.

2.1. Modal Aerosol Module

CAM6 by default utilizes a four-mode MAM (MAM4) (X. Liu et al., 2016) to represent a total of six aerosol species: Aitken (A2: soil dust, sulfate, sea salt, and secondary organic matter), accumulation (A1: sulfate, secondary organic matter, primary organic matter, black carbon, sea salt, and soil dust), coarse (A3: soil dust, sea salt, and sulfate), and a primary carbon mode (A4: primary organic matter and black carbon). These species, represented by separate tracers, are assumed to be internally mixed within the same mode and externally mixed between different modes. Due to the varying physical properties of species (e.g., hygroscopicity, optical properties, and density), this aerosol mixing state is essential for accurately modeling the full aerosol cycle and diagnosing optical properties, which influence radiative effect estimates. In addition, the total number concentration of aerosol species in a mode is also advected as a separate tracer, along with the mass mixing ratio of each species (X. Liu et al., 2016).

The size distribution of each mode assumes a log-normal shape, with the mode parameters listed in Table 1. These parameters are prescribed in the user namelist file, including the globally constant geometric standard deviation (GSD), the initialized geometric mean diameter (GMD) for online predictions, and the range used to constrain the simulated GMD. It is worth noting that a previous study (Li et al., 2022b) adjusted the coarse mode size distribution parameters (GSD and initialized GMD and its range) to those used in CAM5, resulting in large changes in the modeled dust aerosol cycle and improving the representation of the dust size distribution. This adjustment is retained here to better represent the dust aerosol size distribution in CAM6-MAM4. Although dust emission size cut-offs span a broad and physically motivated range, the simulated dry GMDs in MAM are constrained within narrower prescribed bounds. This “discrepancy” arises because emission cut-offs represent the range of particle

sizes that can be emitted as aerosols at the surface, whereas the modal aerosol framework imposes tighter bounds on GMDs to maintain numerical stability and modal integrity under fixed lognormal assumptions.

Processes that determine the removal rate of aerosols from the atmosphere include dry and wet deposition. The dry deposition (e.g., gravitational settling and turbulent removal) rate, calculated in the model via parameterizations, partially depends on the aerosol size (i.e., the predicted GMD and prescribed GSD for each mode). The model we take as default here uses a revised dry deposition scheme (Petroff & Zhang, 2010), compared to that used in the officially released version (L. Zhang et al., 2001). This revised scheme, as previously shown, helps mitigate the overestimated dry deposition velocity of fine aerosols, such as black carbon (Wu et al., 2018) and dust in the fine modes (Aitken and accumulation) (Li et al., 2022b), as tested in CAM5 and CAM6, respectively. The baseline CAM5 and CAM6 configurations used in this study correspond to the officially released versions that participated in the Coupled Model Intercomparison Project Phase 5 (CMIP5) and Phase 6 (CMIP6), respectively. However, all simulations analyzed here include additional developments—most notably mineral-resolved dust and associated physics updates—that were not part of the CMIP production configurations. The results therefore represent targeted sensitivity experiments within the CAM framework rather than CMIP6 simulations.

Wet deposition depends on the relative location of aerosols with respect to clouds and consists of in-cloud and below-cloud scavenging, both of which are applied separately to convective and stratiform precipitation following the standard CAM5 formulation (Neale et al., 2010). The in-cloud scavenging uses cloud properties (e.g., cloud water, precipitation production profiles) to compute aerosol loss rates, scaled by solubility factors that represent the aerosol fraction incorporated into cloud water. Stratiform cloud-borne aerosols—primarily sulfate, sea salt, secondary organic aerosol, and the soluble fractions of organic matter and mineral dust—are treated as fully soluble upon activation (solubility factor of 1.0), whereas non-activated aerosols remain interstitial and are unaffected. Dust activation is governed in part by its prescribed hygroscopicity ($\kappa = 0.068$), which influences the fraction of dust that becomes cloud borne. Convective in-cloud scavenging applies solubility and activation factors that depend on aerosol hygroscopicity but not mode, with an activation factor of 0.40 for dust aerosols, reflecting their relatively weak activation compared to more hygroscopic species (e.g., sea salt). All these parameter values are inherited from the standard CAM5 implementation (Neale et al., 2010) and are not tuned in this study.

The below-cloud scavenging removes interstitial aerosols through impaction and diffusion, with removal rates dependent on solubility factor, scavenging coefficient, and precipitation rate (Neale et al., 2010). CAM6-MAM4 calculates size-dependent scavenging coefficients (Easter et al., 2004) and applies a solubility factor of 0.10, which effectively serves as a tunable parameter. Stratiform cloud-borne aerosols are not subject to the below-cloud scavenging. However, aerosols scavenged at higher altitudes can be resuspended at lower atmospheric levels. In CAM6, the fraction of resuspended aerosol is set equal to the fraction of evaporated precipitation.

A particle's hygroscopic growth or shrinkage depends on its hygroscopicity, dry radius, density, ambient relative humidity, and temperature, following the κ-Köhler theory (Ghan & Zaveri, 2007). This process determines the particle's final wet size and volume at equilibrium under ambient conditions. The volume-averaging mixing rule is then applied to predict the band-averaged (see Li et al., 2021 for band information) complex refractive index of the wet aerosol mixture, based on the relative abundance and complex refractive index of each component (using its dry-state value for aerosols), including water (Ghan & Zaveri, 2007). To parameterize the optical properties of the aerosol mixture, such as single-scattering albedo across different bands, the model uses a look-up table containing Chebyshev polynomial coefficients (see Section 3.1.3 for details on how we generate it) and an interpolation method based on the band-averaged complex refractive index of the wet aerosol mixture (Ghan & Zaveri, 2007).

2.2. Default Dust Modeling Without Mineral Speciation

The default dust emission in the officially released CESM2 relies on the dust entrainment and deposition model (DEAD) (Zender, Newman, & Torres, 2003) in CLM4.5, which simulates the dust mobilization based on the mechanism proposed by Marticorena and Bergametti (1995). This emission scheme was previously updated to a more physically based one (Kok, Mahowald, et al., 2014), shifting emissions to topographic depressions, where abundant erodible sediment accumulates, without using a time-invariant empirical source function such as previously used (Ginoux et al., 2001; Mahowald et al., 2006; Zender, Newman, & Torres, 2003).

Dust emission is initiated when the near-surface friction velocity exceeds the fluid soil threshold friction velocity for saltation, the process by which wind lifts sand particles (100 μm in diameter) and propels them into ballistic

trajectories, ejecting smaller dust aerosol-sized particles into the air upon collision (Kok et al., 2012). This soil threshold friction velocity is determined primarily by near-surface meteorological fields and top 1.0–2.0 cm soil properties such as moisture content, grain size distribution, and land cover (e.g., vegetation) (e.g., Shao, 2008). Vegetation influences dust emissions via the leaf area index (Mahowald et al., 2006) in CLM4.5. When the leaf area index exceeds 0.30 m^2 m^{-2}, vegetation is assumed to fully block the transfer of wind momentum to the surface soil, preventing dust emissions. Below this threshold, the fraction of a grid cell that can emit dust aerosols increases linearly with decreasing leaf area index. The suppression of dust emissions due to soil moisture is activated when the near-surface soil gravimetric water content exceeds a threshold determined by the clay content of the soil. This relationship is represented in the land model using a semi-empirical formulation (Fécan et al., 1998) and the top 10 cm soil gravimetric water content. Observational studies linking wind threshold behavior to soil gravimetric water content typically focus on the top 1.0–2.0 cm of soil, which dries rapidly following precipitation. In contrast, the uppermost soil layer in the model spans 0.0–10 cm and retains moisture longer, introducing inertia not representative of surface conditions and thus uncertainty in the dust emission modeling (Darmenova et al., 2009), which we do not address in this study.

The size distribution of emitted total dust aerosols follows the brittle fragmentation theory (Kok, 2011a), which allocates 0.10%, 1.0%, and 98.9% of dust mass into Aitken, accumulation, and coarse modes, respectively, regardless of the friction velocity at the time of emission (Kok, 2011b). After emission, dust aerosols are transported, interacting with radiation and clouds, and removed from the atmosphere in CAM6.

Evaluations using observations, including in situ measurements and remote sensing retrievals, suggest that compared to the default emission scheme in the officially released CAMs (Zender, Bian, & Newman, 2003), the more physically based emission scheme, along with the updated size distribution of emitted total dust aerosols, maintains or improves accuracy in modeling the dust climatology in previous CAM versions (Kok, Albani, et al., 2014; Li et al., 2022b).

2.3. Mineral-Resolved Dust Modeling

The dust model (Section 2.2) was modified to categorize the single dust tracer into eight separate mineral tracers (Li et al., 2021; Scanza et al., 2015), enabling detailed optical property calculations based on dust mineral composition. The eight minerals include illite, kaolinite, montmorillonite (smectite), iron oxides (hematite and/or goethite), quartz, calcite, feldspar, and gypsum. They represent the most common minerals present in the clay- (soil grain diameter below 2.0 μm) and silt-sized (diameter between 2.0 and 63 μm) soil categories (Claquin et al., 1999).

The distribution of the eight minerals in the clay- and/or silt-sized categories was derived offline from a global soil atlas, based on the mean mineralogy table of Claquin et al. (1999), where mineralogy is inferred from a global atlas of soil type. Additional modifications by Scanza et al. (2015) and Li et al. (2021) include normalizing the mineral fractions within each clay- or silt-sized category for 28 soil types. An equal and opposite adjustment to the illite percentage ensures consistent hematite amounts in both clay- and silt-sized categories. A nearest-neighbor algorithm was then applied to fill the grid cells in the land model for dust emissions. This nearest-neighbor assignment is applied only during the preprocessing step that maps the soil mineral atlas to the CESM grid, ensuring complete mineral coverage over all dust-emitting land surfaces. The conversion of soil mineralogy to dust aerosol mineralogy follows the brittle fragmentation theory (Kok, 2011a), as previously described (Scanza et al., 2015).

Mineral tracers are emitted into the same transport size modes as bulk dust. Minerals are not assumed to be uniformly distributed across particle sizes; instead, the mass fraction of each mineral emitted into a given mode reflects its abundance in the soil clay- and silt-size categories. Consequently, minerals associated with coarser soil material (e.g., quartz) contribute more strongly to coarser dust modes, while minerals enriched in finer soil fractions contribute more to finer modes. Mineral emission fractions are defined such that, within each mode, the sum of all mineral emissions equals the corresponding bulk dust emission, thereby preserving the bulk dust size distribution at emission. The predicted mineral relative abundances then evolve independently during transport and removal, undergoing the same atmospheric processes as dust in the released model version, including advection, deposition, and aerosol microphysics (e.g., coagulation).

All component minerals are assumed to be internally mixed within a mode. Mineral densities are set to values used in a previous study (Li et al., 2021). The scavenging efficiency and hygroscopicity of these minerals are consistent with those prescribed for dust without speciation, as described in Section 2.1. The complex refractive

Table 2
Dust Mode Parameters in the Ten-Mode Modal Aerosol Module (MAM10)

Dust mode	A5 (fine)	A7 (fine/coarse)	A8 (medium coarse)	A9 (super coarse)	A10 (super coarse/giant)
Dust emission size cut-offs (μm)[a]	0.10–1.0	1.0–5.0	5.0–10	10–20	20–70
Geometric standard deviation (GSD)	1.8	1.7	1.5	1.5	1.5
Initialized dry geometric mean diameter (GMD) (μm) (number distribution)	0.56	2.0	5.5	8.6	14
Low and upper bounds for simulated dry GMD (number distribution; μm)[b]	0.36–0.76	1.7–2.4	4.0–6.3	8.3–10	10–18
Emitted mass fraction					
Fractional contribution to total dust	0.0028	0.14	0.19	0.24	0.43
From clay	1.0	0.97 (0.57)[c]	0.87 (0.57)[c]	0.87	0.87
From silt	0.0	0.030 (0.43)[c]	0.13 (0.43)[c]	0.13	0.13

[a]The size categories used here are defined strictly by particle diameter and reflect the modal structure of the aerosol model; they are not intended to imply differences in transport distance or atmospheric lifetime. [b]Lower and upper bounds are applied to constrain the simulated GMD of each dust mode. [c]Values outside parentheses are derived using the brittle fragmentation theory for non-hematite minerals, while values in parentheses correspond to hematite and have been refined.

indices for all component minerals, except iron oxides, are based on Scanza et al. (2015). For iron oxides, an observationally constrained complex refractive index is applied, which improved the accuracy in predicting optical properties of dust aerosols and their relationship with iron oxide content using the volume-averaging mixing rule, compared to other publicly available indices (Li et al., 2024).

3. Updates to Dust Representations in the Model

This section documents the model developments implemented in this study, with a focus on changes to the representation of mineral dust aerosols in CESM2. A central limitation of earlier CESM2 dust configurations described in Section 2 is the use of a small number of aerosol modes, in which a single coarse mode encompasses a wide particle size range and size-dependent processes are applied at a mode-mean diameter. This formulation restricted the model's ability to simultaneously capture the rapid gravitational removal of very large particles and the longer atmospheric residence times of smaller coarse dust. The updates described here address this limitation by extending the modal aerosol framework to explicitly resolve the coarse and giant dust size ranges, thereby enabling size-dependent transport, removal, and radiative processes to operate more consistently across the observed dust size distribution.

We introduce two key enhancements to the mineral-resolved CAM6: additional modes via the new MAM10 to simulate super coarse and giant dust particles, which constitutes the primary model-development advance of this study (Section 3.1), and improved physics to simulate dust emission (Section 3.2). The development of MAM10 in CAM6 builds upon the previous MAM9 and seven-mode MAM (MAM7) frameworks in CAM5 (Ke et al., 2022; X. Liu et al., 2012) without mineral speciation, while the advanced dust emission physics are based on those implemented in CAM6 (Leung et al., 2024), which likewise has no mineral speciation. The first modification primarily involves changes to the atmosphere component, and the second focuses on the land component.

3.1. A New Modal Aerosol Module

MAM10 represents dust aerosols in five distinct transport modes (A5, A7, A8, A9, and A10), as summarized in Table 2. Each of these modes contains two internally mixed species: dust and sulfate. Sulfate is included in the dust modes to represent secondary sulfate coatings formed through sulfuric acid condensation during dust aging, consistent with the internal-mixing assumption of MAM4 (X. Liu et al., 2016). While we do not detail sulfate representations, we note that sulfate has multiple sources (X. Liu et al., 2012), and that sulfate in the coarse modes originates from the condensation of sulfuric acid gas produced by the oxidation of sulfur dioxide, which is either directly emitted or formed via the oxidation of dimethyl sulfide. Sea salt is represented in A1, A2, A4, and A6, separate from dust modes, similar to MAM7 and MAM9 (Ke et al., 2022; X. Liu et al., 2012). Other non-dust aerosol species, such as particulate organic matter and black carbon in the non-dust accumulation mode (A2)

Table 3
Experimental Design

Mode version	Four-Mode Modal Aerosol Module (MAM4)	Ten-Mode Modal Aerosol Module (MAM10)
Dust emission scheme	Kok, Mahowald, et al. (2014); linear dependency on modeled leaf area index and the leaf area index threshold is set as 0.30 m^2/m^2 above which no emission occurs	Leung et al. (2023, 2024) with leaf area index from the Modern-Era Retrospective analysis for Research and Applications version 2 (MERRA2) and increased leaf area index threshold to 1.0 m^2/m^2
Dust size distribution	As in Li et al. (2022b); also shown in Table 1	See Table 2
Dust tuning parameter (dust_emis_fact: inversely linked to dust emission rate)	3.6	0.35
Dust optical depth in the visible band (0.44–0.63 μm)	0.030	0.031
Percentage reduction to gravitational settling velocity of dust aerosol	0.0	50, 75, 85 for A8, A9, and A10, respectively
Simulation period	2007–2011 (one additional year for model spin-up)	2007–2011 (one additional year for model spin-up)
Look-up table for aerosol optical property diagnostics	As in Li et al. (2022b)	Regenerated to accommodate with new dust modes (Section 3.1.3)
Soil mineral atlas	Mineral fractions derived from Claquin et al. (1999) and normalized to unity	Derived from the Earth surface Mineral dust source InvesTigation (EMIT) project following the Algorithm Theoretical Basis Document (ATBD) (see Section 3.4)

aged from the primary carbon mode (A3), are also simulated in MAM10 using the same mode settings as in MAM9.

It is important to note that simulations of the non-dust species in MAM10 are expected to vary from MAM4 due to different size settings and mixing states of dust aerosols with the other species (e.g., sea salt). These distinctions could affect the simulated dust aerosols by modifying dust deposition rates. For example, the internal mixing of sea salt with dust aerosols can increase the hygroscopicity of the mixture, thereby enhancing the wet removal rate of dust aerosols. The simulation of non-dust aerosol species, their climate impacts, and their influence on dust aerosol simulations fall outside the scope of this study.

As in previous MAM versions, each mode is described by three parameters: the GSD, GMD, and volume or mass concentration, detailed in Tables 1 and 2 and the following subsections.

3.1.1. Refinement of Dust Size Distribution

The size distribution of emitted total dust aerosols follows an extended brittle fragmentation theory (Meng et al., 2022), which is better suited to represent the full observed dust size distribution accommodated by the new MAM10 framework than the original formulation of Kok (2011a). This extended formulation allocates approximately 0.68%, 15%, 17%, 24%, and 43% of emitted dust mass into the fine, fine/coarse, medium-coarse, super-coarse, and super-coarse/giant dust modes, respectively, independent of the friction velocity at the time of emission (Kok, 2011b). While the emitted dust size distribution is constrained by available observations for dust with diameters smaller than 10 μm, limited observational evidence exists regarding how the fractional contribution of super-coarse and giant dust varies with friction velocity or soil type (Meyer et al., 2026). For simplicity, we therefore neglect any such dependencies, consistent with the treatment applied to dust with diameters smaller than 10 μm.

The mode parameters in MAM10 (Table 2), along with adjustments to the gravitational settling velocity of dust aerosols (Table 3), are fine-tuned to match the observed size distribution (Formenti & Di Biagio, 2024). The optimized dust aerosol size distribution from Adebiyi et al. (2020), extended to include the giant dust mode (emission size range in geometric diameter: 20–70 μm), supports using a constant GSD of 2.0 across all modes.

However, initial tests with this value failed to match observations near North African dust sources, whereas a subsequent test, reducing the GSD to 1.5 for the three largest dust modes (A8, A9, and A10; Table 2), achieved a better model performance (see Section 7.2.3).

The rationale for adopting a GSD of 1.5, rather than 2.0, which provides the best fit to the observed size distribution using five lognormal modes, likely reflects persistent uncertainties in dust modeling and model-observation comparisons. For example, modeling the evolution of dust size remains inherently challenging. We apply the obtained GSD uniformly in all the calculations requiring this parameter, including diagnostics of dust optical properties. The assumption behind using a constant GSD across different modes globally is that the width of the size distribution remains unchanged between freshly emitted and aged dust aerosols. This approach may not fully capture variations in the GSD, as atmospheric processes (e.g., size-dependent cloud interactions and deposition) can modify the size distribution during transport. A more accurate solution would be desirable as the model development advances with additional measurements of both freshly emitted and aged dust aerosols.

While the mode parameters for dust between 0.40 and 10 μm in diameter are relatively well constrained by observations, those for particles outside this range are more uncertain (Formenti & Di Biagio, 2024). This reduced confidence for the submicron accumulation mode stems from several factors, including contamination by non-dust aerosols (e.g., biomass burning, especially for particles smaller than 0.50 μm in diameter) and assumptions about dust shape that limit the accuracy of the measurements used for size distribution optimization (Dubovik et al., 2000). For the giant dust mode, the uncertainty is mainly due to the scarcity of measurements and instrument limitations. Although AErosol RObotic NETwork (AERONET) retrievals are abundant and capture aerosol mass up to 30 μm in diameter, they are sensitive to assumptions about large particle sizes (Zheng et al., 2024).

Due to challenges in representing the dust size distribution, the model requires a prescribed range of the GMD for each mode to reasonably simulate it. Sensitivity tests without these bounds show that the last four largest dust modes (A7, A8, A9, and A10) tend to merge into a "single" broad mode. The GMDs of the fine/coarse and medium-coarse modes are sensitive to the prescribed upper bounds, while the super-coarse and giant modes are more influenced by the lower bounds. Limited observational data to constrain the simulated diameters for the three largest dust modes (A8, A9, and A10), combined with the use of a globally constant GSD for each mode and the absence of mechanisms to transport dust particles larger than 5.0 μm in diameter, prevents this study from fully capturing the observed dust size dynamics.

3.1.2. Tuning the Gravitational Settling Velocity for Large Dust Particles

The Stokes settling velocity overestimates the settling velocity of particles larger than 20 μm in diameter by more than 10%, primarily because the particle Reynolds number (Re) approaches or exceeds 1.0, the upper limit for which Stokes' law is valid (Stokes, 1851). The magnitude of this error becomes more pronounced with increasing dust particle size. For example, particles of 200 μm in diameter can have a settling velocity bias of up to 60%. To address this issue, a time-invariant Stokes correction factor is applied in CAMs to coarse particles up to a maximum aerosol diameter of 1,000 μm (Zender, Newman, & Torres, 2003), although previous versions of CAM do not simulate aerosol particles of such large sizes. Despite this correction, large dust particles still appear to settle too quickly compared to the real atmosphere, limiting the model's ability to match measured dust size distribution (see discussions in Section 8 for the proposed reasons so far). It is worth noting that the transport of large dust particles follows the standard CAM6 schemes. While vertical turbulent transport may be size-dependent, here we do not implement size-dependent diffusion.

Due to misrepresented or absent mechanisms in the model's dust-related parameterizations, an adjustment, as applied in previous studies (Drakaki et al., 2022; Meng et al., 2022), is used to better simulate super-coarse and giant dust aerosols. A mode-dependent reduction is applied, with larger reductions assigned to progressively larger dust modes, to account for the increasing overestimation of gravitational settling for medium-coarse, super-coarse, and giant particles in modal representations. Specifically, we reduce the settling velocity for the three largest dust modes (A8, A9, and A10) by 50%, 75%, and 85%, respectively (Table 3), to counteract gravitational settling, thereby narrowing the differences in dust size distribution between the model and observations. While more formal alternative methods may exist (see discussions in Section 8), this approach offers a practical compromise to address the overestimation of large dust particle settling velocity in the models until particle transport mechanisms are better understood and incorporated, a critical task beyond the scope of this study. This tuning approach is nonetheless valuable. For applications such as estimating the dust direct radiative effect (a

primary objective of the EMIT mission) a realistic spatial distribution of dust is essential, even when achieving it requires empirical adjustments. Accordingly, this study provides a transparent description of how the CAM dust distribution is derived for the EMIT direct radiative effect application (Li, Mahowald, Obiso, et al., 2025).

Changes in the gravitational settling velocity of large dust aerosols can also influence their wet deposition processes, which we do not quantify separately from the total dust budget estimation, including dry deposition. This interaction arises for two main reasons. First, modifying the dry deposition velocity in one mode can alter simulated dust burdens, which directly affect the wet scavenging rate as a first-order function of dust burden, thereby impacting dust aerosol removal via wet deposition. Second, due to the mode's width, dust number or mass concentrations in one mode can contribute to the total dust mass within the size range represented by neighboring modes. This contrasts with the binned approach, where size bins have fixed boundaries and no overlap between modes.

3.1.3. Parameterization of Aerosol Optical Properties

CAM6 uses parameterized aerosol optical properties to calculate aerosol radiative effects while minimizing computational costs. In this study, we use the approach outlined by Ghan and Zaveri (2007), generating a coefficient look-up table for MAM10. Sensitivity tests by Ghan and Zaveri (2007) suggest that this method reproduces aerosol optical properties calculated by the Mie Theory with errors generally less than 20%, and under most conditions, within 30% of the Mie solution, except when their absolute values are small.

The look-up table, applied to all aerosol modes and species, provides coefficients for total aerosol specific absorption (σ_{abs}; unit: m^{-1}), extinction (absorption plus scattering, σ_{ext}; unit: m^{-1}), and the asymmetry parameter (g) across 14 shortwave bands, as well as specific absorption for 16 longwave bands. We derive the coefficients by fitting Chebyshev polynomials to mass-weighted (m_w) specific optical properties (i.e., $\log(\sigma_{sca}/m_w)$: unit—$m^2\ g^{-2}$, σ_{abs}/m_w: unit—$m^2\ g^{-2}$, and g) based on Mie simulations with seven real (n_r) and 10 imaginary (n_w) components of complex refractive indices that bracket the probable absorption range of aerosols. These components are equally spaced between 1.3–1.6 and 0.0–0.79, respectively. A brief introduction to the parameterization of aerosol optical properties using the Mie Theory is provided in Text S1 in Supporting Information S1, with detailed descriptions available in Ghan and Zaveri (2007).

It is important to note that the Mie Theory cannot be applied to particles with non-spherical shapes for optical property calculations. However, dust aerosols are typically non-spherical (Kalashnikova & Sokolik, 2004) and exhibit complex morphologies (Falkovich et al., 2001), which increase their extinction efficiency (Huang et al., 2023). To address this limitation, we apply shape corrections by increasing the visible-band mass extinction efficiency by 16% for fine dust aerosols (A5 and A7) and by 28% for coarser dust aerosols (A8, A9, and A10), based on previous calculations (Kok et al., 2017) and an extension of the dust emission cutoff geometric diameter to 70 μm. This adjustment is applied only to shortwave bands, as the dust model is tuned to the estimated global visible-band dust optical depth of 0.030 (Ridley et al., 2016), although shape effects may similarly enhance the longwave extinction efficiency (Huang et al., 2023).

3.2. Amendments to Dust Emission Physics

Despite the improvements achieved (Kok, Mahowald, et al., 2014), the physically based scheme previously incorporated into the mineral-resolved CESM2-CAM6 (Li et al., 2022b) (described in Section 2.2) still lacks key physics necessary for accurately predicting dust emission strength and location. This limitation led to the development of a more scientifically comprehensive scheme (Leung et al., 2023) designed for integration into ESMs (Leung et al., 2024). Here, we incorporate this scheme into our mineral-resolved dust model.

The additional physics included in the emission process now accounts for two critical factors. First, intermittency from unresolved instantaneous wind fluctuations, such as turbulence, which occur on timescales (around 1 min or less) smaller than the model's 30-min time step within the near-surface boundary layer. Second, drag partitioning due to surface roughness elements, like vegetation and rocks, that partially absorb wind momentum. This absorption reduces the downward momentum flux available to uplift soil dust particles.

We briefly summarize the key elements below. Texts S2 and S3 in Supporting Information S1 provide additional details on the parameterizations of emission intermittency and drag partitioning due to non-erodible elements, respectively. For further information, see Leung et al. (2023).

Moreover, a global unconsolidated sediments map (GUM) (Börker et al., 2018) is applied as a surface erodibility constraint in the updated dust emission model. This implementation suppresses dust emission from consolidated surfaces, allowing emission only from unconsolidated regions (e.g., loose sands, silts, and dust beds) and spectrally identified by EMIT as potential dust sources.

3.2.1. Emission Intermittency

In ESMs with prognostic dust, accounting for intermittency could be crucial (Comola et al., 2019) to avoid considerable biases in dust emission simulations (Dupont et al., 2013). Saltation intermittency is due to the highly turbulent surface winds that frequently sweep across the dust emission threshold friction velocity, causing multiple sudden initiations and terminations of dust emissions on a timescale of minutes. Theoretical studies indicate that the saltation intermittency effect is further complicated by the fact that there are two threshold friction velocities for dust emission: the fluid threshold required to initiate saltation, and the impact threshold required to sustain saltation after it has been initiated (Bagnold, 1941; Kok et al., 2012). In most schemes, dust emission begins when friction velocity exceeds the fluid threshold but ceases when friction velocity falls below this threshold. However, in practice, emission persists even when friction velocity decreases to a value between the two thresholds, ceasing only when it drops below the impact threshold. This saltation intermittency effect could be important under two conditions where accounting for intermittency can improve dust emission simulations (Kok et al., 2012).

First, when the model surface wind speed is below the fluid erosion threshold, turbulent fluctuations can still initiate saltation and dust emission, which is then sustained until the wind drops below the impact threshold. Second, soil cohesion, while not affecting the impact erosion threshold, considerably increases the fluid erosion threshold (Comola et al., 2019). These conditions typically occur in marginal source regions (e.g., semi-arid areas) due to higher soil moisture than arid regions. Consequently, incorporating the intermittency effect tends to increase dust emissions over these marginal source regions more than over arid regions (Leung et al., 2023).

To include the intermittency effect, a substepping scheme was developed to parameterize the effects of instantaneous wind fluctuations on initiating and ceasing dust emission (Comola et al., 2019). A saltation intermittency factor, ranging between 0.0 and 1.0, is introduced in the updated dust emission scheme (Leung et al., 2023), representing the fraction of time during which saltation and dust emissions are active within a model time step (see Text S2 in Supporting Information). The updated dust emission is then modeled as the product of this intermittency factor and the vertical dust emission calculated by the previous version of the scheme for each model time step. This intermittency parameterization follows Leung et al. (2023) and represents an effective treatment of enhanced dust emission near the threshold friction velocity; it is not intended to provide a complete physical description of turbulent dust emission, which remains challenging (D. Liu et al., 2018) and is beyond the scope of the present study.

3.2.2. Drag Partitioning Due To Non-Erodible Elements

A surface roughness correction factor is applied to the modeled friction velocity to account for drag partitioning effects from rocks or vegetation (Leung et al., 2023), which were either absent or not well represented in CESM versions before that study. The effects of these two elements are calculated separately and then combined using a weighted mean based on the fractional area of each grid cell dominated by rocks or vegetation (see Text S3 in Supporting Information).

The drag partitioning due to rocks is quantified using a semi-empirical equation by Marticorena and Bergametti (1995), with aeolian roughness length provided by satellite retrievals of the backscatter coefficient at 5.3 GHz (Prigent et al., 2005). To separate the roughness map for rocks from vegetation, the minimum value of the monthly aeolian roughness length in a climatological year is used. This map is applied to grid cells where the vegetation area index (the sum of the one-sided leaf area index and stem area index) is less than 1.0 m^2 m^{-2}. The parameterization thus accounts only for photosynthetic vegetation, excluding other types such as plant debris and senescent leaves.

The drag partitioning due to vegetation is parameterized following Pierre et al. (2014), building on Okin (2008), by using a gamma distribution to represent the gaps between plants. This parameterization is straightforward to implement in ESMs, as drag partitioning can be approximated using only the leaf area index. In the simulation

with the updated model here, the leaf area index is taken from the Modern-Era Retrospective analysis for Research and Applications version 2 (MERRA2) (Gelaro et al., 2017).

3.3. Conversion of Soil Mineralogy to Aerosol Mineralogy

The distribution of emitted minerals across five dust aerosol modes is determined using the extended brittle fragmentation theory (Meng et al., 2022) and the method proposed by Scanza et al. (2015). The original brittle fragmentation theory predicts that the emitted particle size distribution follows a power law for dust particle diameters (D_d) between 2.0 and 10 μm, with emission outside this range determined by the size-crack propagation length (λ). In contrast to Scanza et al. (2015), our calculation of the emitted mineral distribution employs the bulk dust distribution derived by Meng et al. (2022), which accounts for the dependence of the size-crack propagation length on the diameter of soil aggregates (diameter D_{agg}), in addition to the fully dispersed soil size distribution used in Kok (2011a) and Scanza et al. (2015). This new approach yields a mineral size distribution consistent with the bulk dust distribution used in our model. However, the dispersed soil size distribution is treated as a free parameter, determined by fitting the emitted dust size distribution to observations. The resulting soil particle distribution is skewed toward finer sizes, potentially overrepresenting the clay-sized category relative to the parent soil. In contrast, minerals more evenly distributed across both clay- and silt-sized categories, such as iron oxides, are less sensitive to the assumed soil size distribution.

Following Meng et al. (2022), Equation 1 expresses the size-crack propagation length which is proportional to the diameter of the fragmented soil dust aggregate:

$$\lambda = f_\lambda D_{agg}, \tag{1}$$

where f_λ, the ratio of the size-crack propagation length to the dust aggregate diameter, is set to 0.15.

The normalized emitted mass (M_d) particle size distribution accounting for soil aggregation is given by Equation 2:

$$\frac{dM_d}{dlnD_d} = \frac{D_d}{C_m}\left[1 + \mathrm{erf}\left(\frac{\ln(D_d/\overline{D_s})}{\sqrt{2}\ln(\sigma_s)}\right)\right]\int_0^\infty \exp\left(-\frac{D_d}{f_\lambda D_{agg}}\right)^3 P_{agg}(D_{agg})\,dD_{agg}, \tag{2}$$

where erf is the error function, and C_m is a normalized constant ensuring unit integral of Equation 1 over the diameter range of 0.10–70 μm. The size distribution of fully dispersed soil is approximated by a lognormal distribution with a volume median diameter $\overline{D_s} = 1.13 \pm 0.58$ μm and a GSD $\sigma_s = 1.9 \pm 0.25$. The size distribution of fragmented soil dust aggregates is also modeled as a log normal distribution with a volume median diameter $\overline{D_{agg}} = 127 \pm 47$ μm and a GSD $\sigma_{agg} = \sim 3.0 \pm 1.0$:

$$P_{agg}(D_{agg}) = \left[\frac{1}{D_{agg}\ln(\sigma_{agg})\sqrt{2\pi}}\right]\exp\left[-\frac{\left(\ln(D_{agg}/\overline{D_{agg}})\right)^2}{2(\ln(\sigma_{agg}))^2}\right]. \tag{3}$$

The emitted mass fraction of mineral i ($M_{d,i}$) in different dust modes, arising from clay-sized ($M_{c,i}$) or other-sized ($M_{o,i}$) soil category, is computed by integrating either Equation 4 for the fine and fine/coarse dust mode or Equation 5 for larger dust modes. The integration bounds correspond to the mode cutoff sizes listed in Table 2:

$$\frac{dM_{d,i}}{dlnD_d} = M_{c,i}\frac{dM_d}{dlnD_d} \text{ for } D_d \le 2\ \mu m, \tag{4}$$

$$\frac{dM_{d,i}}{dlnD_d} = M_{c,i}\frac{dM_d}{dlnD_d} + M_{o,i}\frac{D_d}{C_m}\left[\mathrm{erf}\left(\frac{\ln(D_d/\overline{D_s})}{\sqrt{2}\ln(\sigma_s)}\right) - \mathrm{erf}\left(\frac{\ln(2/\overline{D_s})}{\sqrt{2}\ln(\sigma_s)}\right)\right] \times \int_0^\infty \exp\left(-\frac{D_d}{f_\lambda D_{agg}}\right)^3 P_{agg}(D_{agg})\,dD_{agg}, \text{ for } 2\ \mu m < D_d \le 70\ \mu m \tag{5}$$

3.4. The EMIT Soil Mineralogy Atlas

EMIT detects 10 soil minerals (illite, kaolinite, smectite, hematite, goethite, calcite, gypsum, chlorite, dolomite, and vermiculite) using their spectral signatures with an advanced shortwave and near-infrared imaging spectrometer (Thompson et al., 2024) from its vantage point on the International Space Station (ISS) (Green et al., 2020). Mineral identification is conducted at the instrument's native spatial resolution of 60 m, employing the Tetracorder linear feature-matching algorithm (Clark et al., 2024) to interpret surface reflectance. Mass fractions are subsequently estimated using a Hapke-like radiative transfer model (Hapke, 1981), which accounts for scattering and reflection within approximately the top centimeter of soil (Clark & Roush, 1984; Clark et al., 2024), the primary source region for dust emission.

To derive size-resolved mineral mass fractions in emitted aerosols, it is necessary to estimate the distribution of minerals across soil particle sizes. We partition EMIT-derived mineral abundances into the clay- (diameters $\leq$2.0 μm) and silt-sized (2.0–50 μm) categories based on established empirical relationships informed by soil texture data, Food and Agriculture Organization (FAO) soil classification maps, and auxiliary constraints, including observed iron oxide concentrations (Perlwitz et al., 2015a) and AERONET-retrieved dust single-scattering albedo (Obiso et al., 2024). Iron oxides are assumed to be uniformly distributed across soil particle sizes.

A comprehensive description of the methodology used to generate the mineral atlas is available in previously published documentation (P. G. Brodrick, Clark, et al., 2023; Clark et al., 2024; Okin et al., 2023). The publicly released EMIT soil mineral atlas is archived at National Aeronautics and Space Administration (NASA)'s Distributed Active Archive Center (DAAC) (P. G. Brodrick, Okin, et al., 2023).

EMIT soil mineralogy used in this study is derived using Tetracorder expert system 5.27c1 (Clark, 2024; Clark et al., 2024), which has known deficiencies, including misidentifying some nano-hematite-nano-goethite mixtures as jarosite. Thus, the total hematite abundance could be under-reported by the EMIT delivery used for this study. The EMIT team is working on a new reflectance model, and this known deficiency has been mitigated in newer versions (Tetracorder expert system 5.27e1 and later) and the EMIT team will continue to refine the global mineral atlas.

The EMIT retrievals are made across latitudes between 51.6°S and 51.6°N. We mask areas where there is solid rock using GUM (see Section 3.2). High-latitude dust sources exist (Groot Zwaaftink et al., 2016; Meinander et al., 2022). Although their contribution to the global mean annual dust direct radiative effect is minor due to small dust loadings, limited vertical extent, low surface temperatures, and reduced solar irradiance at high latitudes, they can considerably impact regional climates by interacting with clouds (Shi et al., 2021), glaciers, and land or ocean ecosystems (Bullard, 2017). To account for these sources and fill gaps in areas where the EMIT soil atlas provides no data, soil mineralogy from Claquin et al. (1999) is applied.

For our dust model, chlorite, vermiculite, and kaolinite are grouped and collectively transported as kaolinite, using the physical properties of kaolinite. Initial tests indicate that different combinations (e.g., combining chlorite, vermiculite, and illite, and using the physical properties of illite) have a negligible impact on dust direct radiative effect calculations, given the smaller optical property differences among them compared to their differences with iron oxides, particularly in the visible band. Similarly, hematite and goethite are combined and treated as iron oxides due to the limited availability and questionable accuracy of complex refractive index for goethite (Warren et al., 2019). The constrained complex refractive index, which accurately captures the optical properties of dust aerosols and their relationship with iron oxide content in the shortwave spectral range with the combined iron oxides (Li et al., 2024), is applied to the total iron oxide component.

4. Model Configuration

CAM6 with either MAM4 or MAM10 is configured with sea surface temperature prescribed from measurements, with the atmosphere coupled to active land and sea ice models, and to data ocean and slab glacier models. Two simulations (Table 3), both tuned to have almost identical global visible-band dust optical depth (0.030), are conducted to quantify the modeled dust cycle, allowing for a thorough evaluation of the new and old dust models and inter-model comparisons. Therefore, one simulation utilizes the new model with all implemented changes introduced in Section 3, while the other uses the old model introduced in Section 2 with the observationally constrained complex refractive index for simulated iron oxide aerosols. Both simulations are performed at a

horizontal spatial resolution of 1.25° × 0.9° (longitude by latitude) with 56 vertical layers up to 2.0 hPa with offline meteorological fields (air temperature, horizontal wind, and relative humidity) nudged toward the MERRA2 reanalysis data at a 6 hr relaxation timescale for the period 2006–2011 (only the last five-year results are used for data analysis; the first year is taken as model spin-up). Anthropogenic emissions are from the CMIP6 inventory for the year 2000 (Eyring et al., 2016).

5. Observational Data for Model Performance Evaluation

5.1. Dust Aerosol Size Distribution

We utilize previously compiled and harmonized measurements of size distribution (Formenti & Di Biagio, 2024) for freshly emitted dust (residence time less than 1.0 day), as well as dust following medium (1.0–4.0 days) and long (more than 4.0 days) range transport. This classification includes 12, 36, and 10 locations for short-, medium-, and long-range transported dust, respectively.

The compilation comprises 58 data sets collected from literature published over the past 50 years. These data sets were gathered at various locations using different measurement techniques, including microscopy, Coulter multisizers, optical particle counters, optical array probes, and mobility particle sizers. They feature diverse operational size definitions (e.g., optical, projected-area, aerodynamic, and geometric), sampling concentrations and size information (e.g., resolutions and ranges). Such variability complicates accurate and comparable analysis of dust size distributions across sources and transport stages, posing challenges for model evaluation. To address these inconsistencies, Formenti and Di Biagio harmonized the data at four levels (Levels 0, 1, 2a, and 2b). Detailed documentation of the data set is provided in Formenti and Di Biagio (2024).

This study uses their Level 2b data to evaluate modeled dust size distributions. This data set is derived through three key steps: (a) interpolating original data from publications over a common size range with equi-logarithmically spaced diameters; (b) renormalizing the interpolated data so that the integral equals unity over a defined diameter range, enabling direct comparison of size distribution shapes rather than absolute values; and (c) harmonizing observed particle diameters by converting them to a common equivalent geometric diameter that accounts for dust asphericity. These procedures ensure a robust and consistent data set that accounts for inherent differences in dust size distribution measurements, facilitating a better understanding of dust particle size dynamics across different transport stages and a consistent comparison of modeled dust size distributions.

5.2. Dust Optical Depth and Deposition Flux

To evaluate our simulated visible-band dust optical depth, we compare it against AERONET retrievals (aerosol optical depth Version 2 Direct Sun Algorithm, Level 2.0) at the wavelength of 0.50 μm that were postprocessed by Albani et al. (2014). The postprocessing includes rigorous data quality control procedures and station selection criteria based on the dominance of dust optical depth in the reported total aerosol optical depth at the wavelength of 0.50 μm (Albani et al., 2014). For each station, the following criteria were applied. First, only months with at least 10 days of valid observations were retained. Second, a climatological annual cycle was constructed using weighted monthly means. Third, only stations with complete coverage for all 12 months and an annual mean Ångström exponent (0.50 μm) below 1.2 were retained. For these stations, the climatological total aerosol optical depth at 0.50 μm was computed using weighted averages.

The dust deposition flux data utilized in this study were originally compiled by Albani et al. (2014) from various sources (Ginoux et al., 2001; Lawrence & Neff, 2009; Mahowald et al., 2009; Tegen et al., 2002) for present-day climate conditions. Reported mass fractions of dust particles smaller than 10 μm in diameter are used to estimate the total dust deposition flux, including contributions from coarser particles, for comparison with the total flux simulated by both MAM versions.

5.3. Elemental Aluminum Concentration

Elemental aluminum, often found in mineral dust aerosols associated with aluminosilicate, is widely used to identify mineral aerosols within an aerosol population (Formenti et al., 2001; Measures & Vink, 2000; Prospero et al., 2001). We compare elemental aluminum particulate matter derived from simulated minerals with aero-dynamic diameters of up to 2.5 μm ($PM_{2.5}$) and 10 μm (PM_{10}) to newly compiled data from Mahowald

et al. (2025). This data set synthesizes a wide range of mass measurements for $PM_{2.5}$ and PM_{10} aerosol particles from the literature and public health databases, including surface measurements from major dust receptor sites (e.g., Barbados), thereby providing an implicit evaluation of modeled surface dust concentrations.

The cutoff size at 2.5 μm or 10 μm is established according to aerodynamic diameter guidelines, which inform inlet design in reference methods. These $PM_{2.5}$ and PM_{10} values correspond to $PM_{1.6}$ and $PM_{6.9}$, respectively, in geometric space, where aerosol size is defined in our model. We consider this difference in size concept when preparing the model results for comparison, following J. S. Reid et al. (2003), using a dynamic (aerodynamic) shape factor of approximately 1.5.

5.4. Mineral Aerosols

We assess modeled mineral fractions in surface concentrations and deposition fluxes using data previously compiled at 154 locations (Perlwitz et al., 2015a, 2015b), with dust primarily transported from North Africa, the Middle East, and Asia. This data set includes observations from individual points and averages along ship tracks, with sampling periods ranging from days to years, spanning the late 1960s to the 2000s. For details on sample numbers, standard deviations, sampling periods, size ranges, locations, and vessel tracks, see Perlwitz et al. (2015a, 2015b) and references therein. Although most studies in the compilation aimed to measure mineral fractions from dust aerosols (e.g., by extracting dust with polycarbonate or quartz microfibers, cellulose filters, or other filters, or by selecting dust-heavy episodes), various sources of error still exist, which may affect the interpretation of the model-observation comparison.

To evaluate the model's ability to simulate dust mineral composition, we compare model results with observed minerals filtered by Gonçalves Ageitos et al. (2023) to exclude potential anthropogenic contamination by aerosols from industrial activities and combustion processes (Chen et al., 2012; Luo et al., 2008). Observed minerals are mapped to model components, recalibrating mass fractions and standard deviations to account for unrepresented species (e.g., grouping all iron oxides as hematite). The interannual variability of mineral fractions is considered low, enabling comparison between observed values and modeled multi-annual means (Perlwitz et al., 2015a). Model outputs are matched to observations in time (monthly climatology), space, and size by collocating resolved size distributions at corresponding locations and times. For MAM4, only observations with particle sizes smaller than 10 μm in diameter are retained, while broader size ranges are used for MAM10 following Gonçalves Ageitos et al. (2023). Here, we additionally include model-observation comparisons for dust particles larger than 20 μm in diameter. Text S4 in Supporting Information describes in detail how the mineral fraction data set is used.

EMIT provides total mineral abundances in soils but does not resolve their size distribution. It also does not directly retrieve quartz and feldspar. The first version of the EMIT-derived soil map for use in mineral-resolved models, including this study, incorporates pre-EMIT soil mineral atlases and empirical relationships that rely on soil texture data to describe the partitioning of quartz and feldspar, as well as the size distribution of calcite. In order to minimize the impact of these assumptions on model-observation comparisons, we group quartz, feldspar, and calcite simulated by MAM10 into a single category for comparison with observations.

6. Statistical Metrics and Limitations in Model-Observation Comparison

We assess model performance in simulating dust aerosol mineralogy by comparing modeled and observed mineral composition (e.g., ratios of minerals both modeled and observed) and size distribution at corresponding locations and times, using monthly climatology. The modeled dust size distribution is evaluated using monthly climatology, whereas comparisons involving elemental aluminum, dust optical depth, and total dust deposition flux are based on annual means, except when assessing their seasonal cycles, which are evaluated on a monthly basis. For most model-observation pairs, we compute (normalized) mean bias, (normalized) root mean square error, or Pearson correlation coefficients in space or time. Statistical significance of the correlations is tested at the 95% confidence level.

Although model outputs are selected to align as closely as possible in both space and time with available measurements, several potential limitations in the model-observation comparison remain and may affect the interpretation of results, as previously summarized (Li et al., 2022b). These limitations include the following aspects:

First, temporal mismatch. Observational campaigns often span only a few days to weeks, while model results are reported as monthly means. Although we compare monthly climatology, this discrepancy may introduce

uncertainties, particularly given the episodic nature of dust events. The short duration of measurements may not reliably represent climatological conditions, and this mismatch is a common issue across all model-observation comparisons presented in this study. We do not quantify the uncertainty introduced by this limitation.

Second, differences in spatial representativeness. Model outputs reflect averages over grid cells that can span hundreds of kilometers, whereas observational data, such as those from ground stations or aircraft, capture dust properties at much finer spatial scales. This difference in spatial sampling volumes can lead to discrepancies, particularly in regions with strong spatial gradients in dust concentrations.

Third, potential bias in data site selection. Some AERONET site selections are based on modeled aerosol fields, which may not accurately reflect actual optical depth conditions for both dust and non-dust aerosols. This introduces potential bias into the validation process.

Fourth, observational uncertainties. Observational data sets themselves are subject to errors. For example, AERONET aerosol optical depth retrievals may be affected by cloud-screening algorithms (Evan et al., 2022; Levy et al., 2010), and postprocessing procedures applied to dust size distribution data from different field campaigns (Section 5.1) can introduce additional uncertainties (Formenti & Di Biagio, 2024).

Fifth, inconsistencies in mineral types between the model and observations, as well as differences in the number of observation points used for MAM4 and MAM10. Modeled mineral fractions are collocated with observations in time (monthly climatology), space (nearest model grid cell), size, and mineral composition. For the compositional comparison, only minerals present in both the model and observations at a given site are considered, with uncommon minerals excluded rather than dropping the site entirely. This approach maximizes the number of usable observational points per mineral, as not all sites report all modeled minerals. However, it introduces discrepancies in relative mass fractions at sites where the set of modeled minerals differs, for example, between pre-EMIT (Claquin et al., 1999) and EMIT simulations, where chlorite, vermiculite, and kaolinite are grouped and collectively simulated as kaolinite. Additionally, the distinct size ranges represented by MAM4 and MAM10 result in different subsets of valid observational data for each model. As a result, the statistical metrics reflect not only differences in model performance for comparable size ranges but also artifacts introduced by these inconsistencies, complicating direct comparisons between MAM4 and MAM10 in reproducing observed mineral mass fractions.

7. Results

This section evaluates the impacts of the expanded, size-resolved dust aerosol representation introduced in Section 3, with particular emphasis on the explicit treatment of super-coarse and giant particles. We begin by presenting the simulated global annual dust budget climatology (Section 7.1), which establishes the baseline effects of the revised modal framework on dust emission, transport, and removal. Model performance is then assessed against observations across key aspects of the dust life cycle, including annual-mean climatology, seasonal variability, size distribution, and mineral aerosol composition (Section 7.2). Building on these evaluations, Section 7.3 quantifies changes in size-resolved dust fields attributable to the new modal structure, and Section 7.4 examines the contribution and climatic role of dust particles with diameters larger than 10 μm. Collectively, these analyses elucidate how the structural modifications to the dust aerosol framework propagate into measurable differences in simulated dust budgets, transport pathways, and particle-size-dependent behavior.

7.1. Simulated Global Annual Dust Budget Climatology

With a globally averaged visible-band dust optical depth of approximately 0.030 following the dust model tuning (Table 3), the inclusion of dust particles larger than 10 μm in diameter increases the simulated annual global dust budget. During the 2007–2011 period, MAM10 simulates higher global dust emission, deposition (9,500 vs. 2,900 Tg year^{-1}), and loading (40 vs. 24 Tg) than MAM4. The inclusion of super-coarse and giant dust particles enhances dry deposition more than wet deposition, increasing the dry-to-wet deposition ratio. This disparity primarily results from the stronger gravitational settling of coarser dust particles, whose deposition predominantly occurs in arid regions with low precipitation (see Section 7.3). Table 4 provides further details on the distribution of simulated global dust quantities across different sizes/modes.

The disproportionately large deposition (or emission) relative to loading in MAM10, compared to MAM4, is primarily due to the short lifetime of super-coarse (1.1 days) and super-coarse/giant dust particles (0.33 days) (i.e.,

Table 4
Simulated Global Annual Mean Dust Quantities in the Ten-Mode Modal Aerosol Module (MAM10) (Years: 2007–2011)

Mode information	Total; <10 μm; <20 μm	A5 (fine)	A7 (fine/coarse)	A8 (medium coarse)	A9 (super coarse)	A10 (super coarse/giant)
Emission/deposition (Tg year^{-1})	9,500; 3,100 (33% of total); 5,400 (57% of total)	100	1,400	1,600	2,300	4,100
Loading (Tg)	40; 30 (75% of total); 36 (90% of total)	1.9	14	13	7.0	3.5
Lifetime (days)	1.5	11	3.6	2.9	1.1	0.32
Optical depth in the visible band (0.44–0.63 μm)	0.031; 0.0305 (98% of total); 0.0317 (~100% of total)	0.0073	0.016	0.0072	0.0012	0.00028
Visible-band mass extinction efficiency (m^2 g^{-1})	0.40	2.0	0.58	0.28	0.087	0.041

Note. In the second column from the left, numbers in parentheses, if present, indicate the global percentage contribution of dust larger than 10 or 20 μm in diameter to size-integrated dust budgets.

due to differences in particle size distribution). This shorter lifetime of larger particles, combined with the reduced sensitivity of visible-band dust optical depth to larger particles because of their low visible-band mass extinction efficiency (e.g., A5: 2.0 m^2 g^{-1} vs. A10: 0.041 m^2 g^{-1}: the much larger mass of coarser particles partly counteracts this effect; and MAM10: 0.40 m^2 g^{-1} vs. MAM4: 1.3 m^2 g^{-1}), and dust tuning toward a global mean visible-band dust optical depth of 0.030 (Tables 3 and 4), collectively explains why MAM10, despite simulating substantial increases in the dust loading and emission, maintains a global mean visible-band dust optical depth comparable to MAM4.

Particularly, our diagnosed dust quantities for a cutoff size of 10 μm in diameter, based on the simulated size distribution of aged dust, suggest that the higher dust loading in MAM10 compared to MAM4 primarily results from dust particles between 2.0 and 10 μm in diameter. Dust particles larger than 10 μm account for 10 Tg (25% of total dust loading), while dust smaller than 10 μm accounts for 30 Tg (75% of total dust loading) in MAM10, which is 25% higher than in MAM4. The high loading within the 2.0–10 μm geometric diameter range, which may partially explain the overestimated surface elemental aluminum with aerodynamic diameters between 2.5 and 10 μm (see Section 7.2.1), primarily results from the reduced simulated settling velocity of medium-coarse dust particles in MAM10 (Table 3). This high loading in the 2.0–10 μm geometric diameter range, accompanied by a slight compensatory reduction in absolute dust mass for particles smaller than 2.0 μm, mainly reflects the reduced visible-band mass extinction efficiency of dust aerosols in this size range in MAM10. The reduced efficiency, in turn, arises from the model's size distribution parameters for both emitted and transported dust, which are shifted toward coarser particles, thereby lowering visible-band extinction efficiency relative to MAM4. As a result, MAM10 requires a higher dust emission rate (implemented through a lower dust emission tuning factor, which is inversely related to the emission rate; Table 3) to maintain the global mean visible-band dust optical depth at approximately 0.030.

We also compare the simulated dust quantities with the inverse modeling results of Kok et al. (2021a, 2021b) for dust diameters smaller than 20 μm. MAM10 simulates a global mean dust emission of 5,400 Tg year^{-1} for particles smaller than 20 μm in diameter, which falls within the broad range of 3,400–9,100 Tg year^{-1} estimated by Kok et al. (2021a, 2021b). However, the simulated dust loading (36 Tg) is 20% higher than the upper range of 22–30 Tg reported by Kok et al. (2021a, 2021b). This indicates that MAM10 probably overestimates the amount of dust particles smaller than 20 μm in diameter, despite its simulated size distribution comparing well with observations (see Section 7.2.3). To match the dust mass within that size range, tuning the global visible-band dust optical depth from 0.031 to 0.025, which still falls within the observational range of 0.025–0.035 (Ridley et al., 2016), might be a good practice if the visible-band mass extinction efficiency and dust size distribution remain unchanged. As the model-observation agreement on the dust size distribution can still be improved, a second possible approach is to further refine the dust size distribution and gravitational settling velocity, which might help reduce the likely overestimation of dust mass compared to Kok et al. (2021a, 2021b). Another possible approach is to increase the impact of dust particle asphericity on visible-band mass extinction efficiency. This impact is probably underestimated in our model, which may partially explain the overprediction of dust particles smaller than 20 μm by MAM10 relative to Kok et al. (2021a, 2021b).

We did not apply an adjustment in the global dust mass/loading for the present study for two primary reasons. First, simulated dust mass is not the focus but rather one of several dust-related quantities we aim to represent reasonably. Second, this adjustment reflects a pragmatic compromise, as the visible-band dust optical depth is more directly constrained by observations than dust loading, which is inferred indirectly.

7.2. Model-Observation Comparison

7.2.1. Annual Mean Dust Cycle Climatology

The new MAM10 reproduces observed dust cycle within an order of magnitude at most sites while maintaining MAM4's accuracy for dust particles smaller than 10 μm in diameter (Figure 1). This new model provides limited improvement in capturing the overall climatology of visible-band dust optical depth and dust deposition.

Across different regions, the combined changes to CAM6 result in varying degrees of accuracy in reproducing the observed dust cycle compared to the earlier model version (Figure 1). Simulated dust deposition aligns more closely with observations in some regions (e.g., the South Pacific) but shows larger discrepancies in others (e.g., North Indian) (Figure 1). At high latitudes, while suffering from limited data for comparison, both new and old models likely systematically overestimate dust deposition fluxes (Figure 1). This overestimation, which exceeds a factor of two, does not occur in low-to-middle latitude regions (Figure 1). Given the low dust emissions at high latitudes, particularly in the Southern Hemisphere, this discrepancy suggests that the new model, like MAM4, may transport dust from low-latitude source regions likely too efficiently to high latitudes (Figure 1). Consequently, the underestimation of surface dust concentrations and overestimation of deposition observed at several locations, such as near El Djouf and the Antarctic that are present in MAM4 (Li et al., 2022b) and earlier versions of CAM: BAM in CAM version 4 (CAM4) and three-mode MAM (MAM3) in CAM5 (Albani et al., 2014), are still evident in MAM10 (Figure 1). This phenomenon remains particularly evident at sites like King George in the Antarctic (62°S, 58°W) (Figure 1b) compared to that in MAM4 (Li et al., 2022b), where previous studies using observations combined with multiple model ensembles, including an earlier version of CAM4, have reported similar findings (Kok et al., 2021a, 2021b).

The new model does not achieve improvements in representing the spatial variation of surface elemental aluminum with aerodynamic diameters smaller than 2.5 μm (Figure 2). It overestimates that at more observational sites than MAM4 (Figure 3c vs. Figure 3d), more specifically between 2.5 and 10 μm. The cause of this overestimation is unclear. If the model-observation comparison for diameters smaller than 2.5 μm and both data are reliable, a probable explanation could be insufficient vertical transport of dust likely due to the process split issue (Wan et al., 2024) in the model (dust dry deposition is applied immediately after emission and then turbulence mixing), which tends to cause dust to unduly accumulate in the bottom model layer. The likely overestimation of dust mass between 2.0 and 10 μm in geometric diameter, as inferred in Section 7.1 compared to Kok et al. (2021a, 2021b), may also partially explain this overestimation.

The persistent discrepancies between modeling and observations highlight uncertainty in modeling the dust cycle and in model-observation comparisons, influenced by multiple factors summarized in Section 6 and by a previous study (Li et al., 2022b), for which we still lack sufficient information to address. Here, we highlight two additional factors beyond.

First, a known yet unquantifiable error source stems from sparse station-based measurements available for model-observation comparison, particularly in dust source regions. This limitation biases dust aerosol emission modeling, likely leading to overestimated emissions over North Africa (Li et al., 2022b), which remains evident in MAM10, due to the global tuning to achieve a mean visible-band dust optical depth of approximately 0.030. Thus, regional refinement of dust emission might be necessary.

Second, the available measurements themselves are subject to uncertainty, such as those related to deposition (Mahowald et al., 2005) and surface elemental aluminum concentrations (Mahowald et al., 2025). Post-processing procedures applied to reported measurements by original studies likely introduce further uncertainties, as noted for dust size distribution harmonization (Formenti & Di Biagio, 2024).

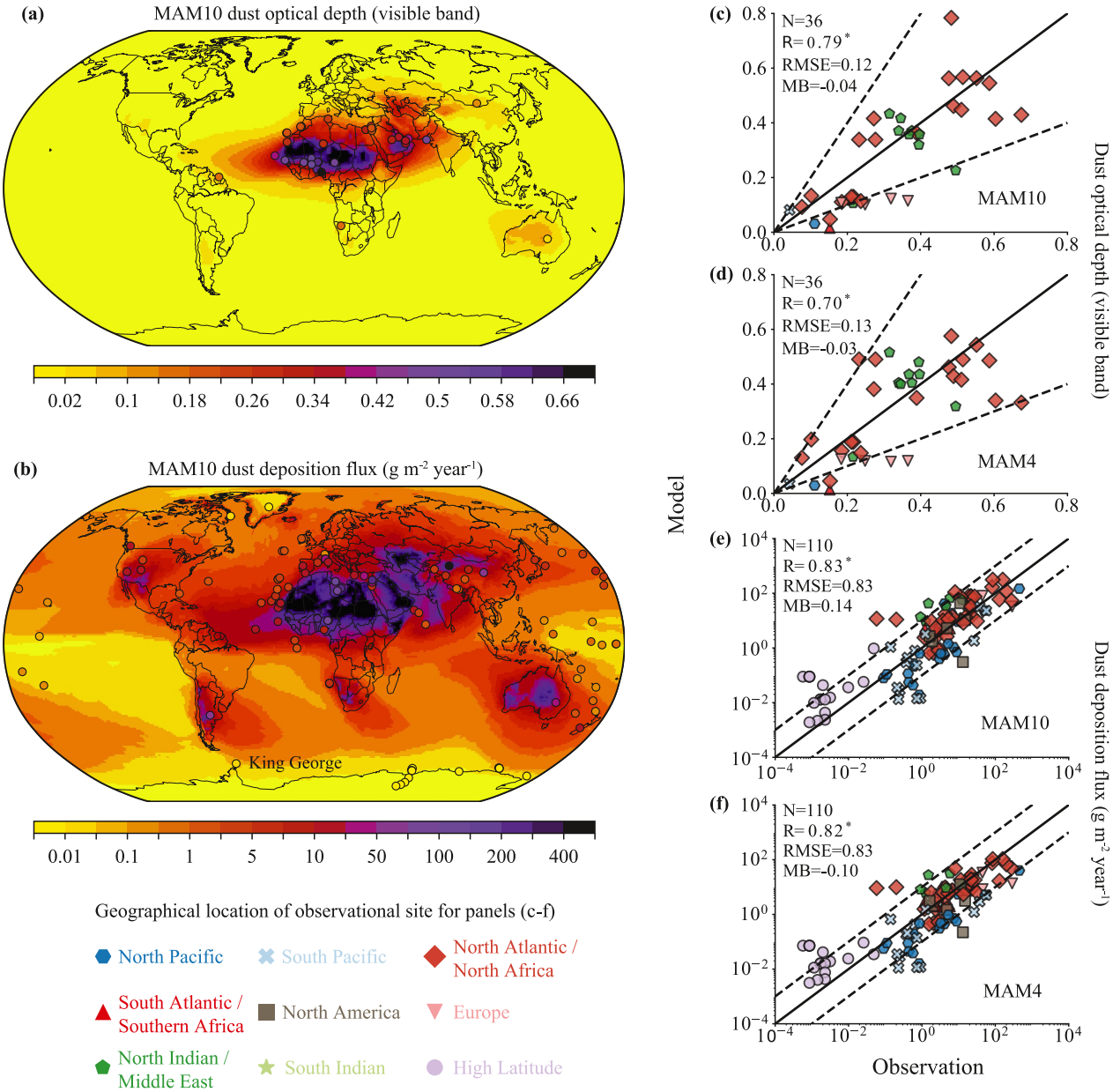

Figure 1. Comparison of simulated total dust quantities with observational data (total number: N) previously compiled (Albani et al., 2014). Panels (a), (c), and (d) show dust optical depth in the 0.44–0.63 μm band, while panels (b), (e), and (f) present deposition fluxes. The deposition fluxes represent values for dust particles with geometric diameters smaller than 10 μm. Black solid lines in scatter plots indicate the one-one line, and dashed lines show a factor of 2.0 (panels c and d) or 10 (panels e and f) difference. Model (MAM10: panels a–c, and e; MAM4: panels d and f) performance metrics include Pearson's correlation (*R*; "*" indicates significance at the 95% confidence level), root mean square error (RMSE; same units as the corresponding dust quantities), and mean bias (MB; same units as the corresponding dust quantities), calculated in the logarithmic space for deposition fluxes and in the normal space for dust optical depth. Table S1 in Supporting Information S1 provides the definition of the geographical regions.

7.2.2. Seasonality of Dust Aerosols

Given the importance of simulating dust seasonality, which interacts with other Earth system components like ocean and land biogeochemistry, we assess the model's ability to reproduce dust seasonality in Figure 4 using previously compiled climatologically monthly mean data for AERONET dust optical depth at the 0.55 μm and surface concentrations (Albani et al., 2014).

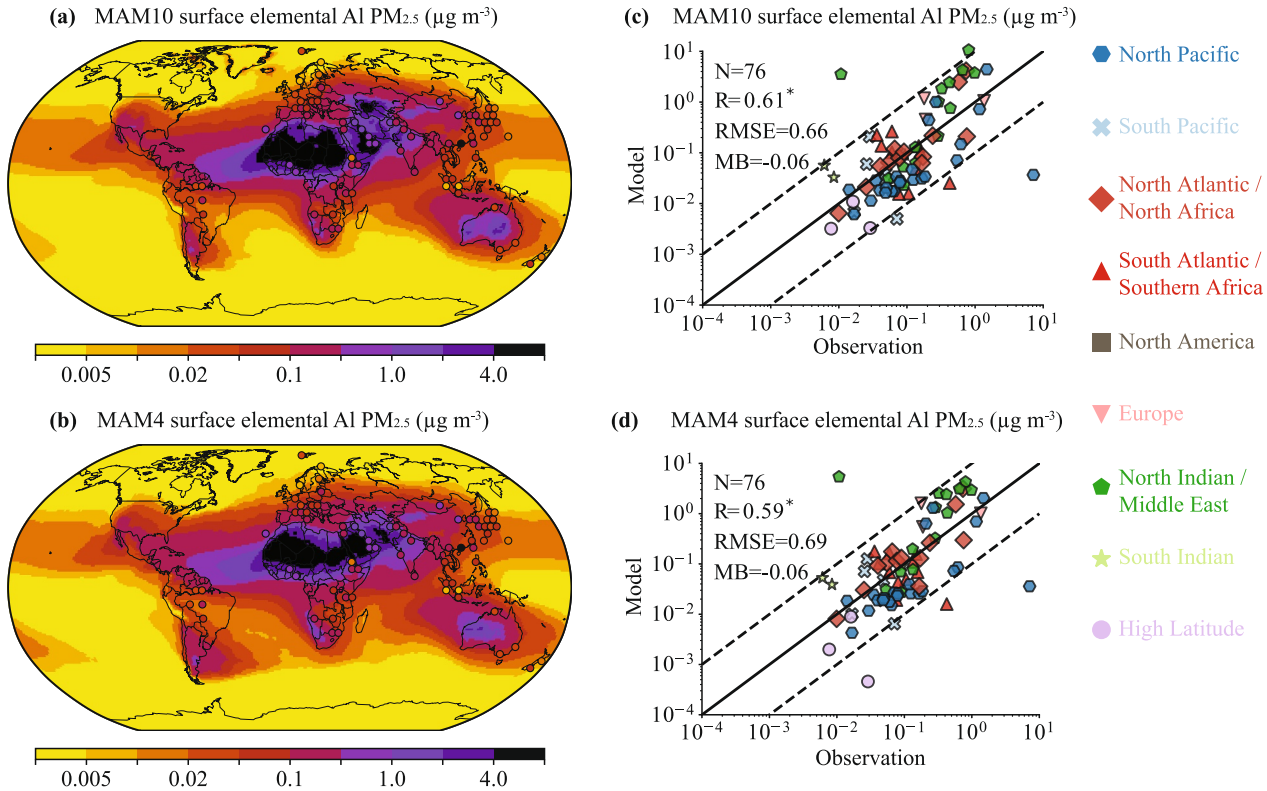

Figure 2. Derived surface elemental aluminum (Al) concentrations based on simulated minerals compared to observations (total number: *N*) previously compiled (Mahowald et al., 2025) with aerodynamic diameters smaller than 2.5 μm (Particular Matter: $PM_{2.5}$). Panels (a) and (c) correspond to MAM10, and panels (b) and (d) to MAM4. Observational data are remapped onto a 4° × 4° regular grid, reducing the data set to 76 points for better visualization and model-observation comparison. Model performance metrics include Pearson's correlation (*R*; "*" indicates significance at the 95% confidence level), root mean square error (RMSE; same units as the corresponding dust quantities), and mean bias (MB; same units as the corresponding dust quantities), calculated in the logarithmic space. Table S1 in Supporting Information S1 provides the definition of the geographical regions.

MAM10 simulates different seasonal cycle amplitudes of visible-band dust optical depth (Figure 4a) and surface concentrations (Figure 4b) from MAM4, although the temporal correlations are similar between the two models, better for dust optical depth than for the surface concentrations. Both models capture the observed seasonal phase (e.g., the month of the maximum or minimum value) of the dust optical depth and surface concentrations variability at some sites but not at others, and MAM10 does not show improved phase agreement relative to MAM4 (Figures S1-S3 in Supporting Information S1). Overall, the new model slightly improves the simulated seasonal amplitude of the visible-band dust optical depth (Figure 4a), while slightly degrading that for the surface concentrations (Figure 4b). This improvement is primarily attributed to the inclusion of drag partitioning in the updated dust emission scheme (Leung et al., 2023), which reduces dust emission during peak summer while having a minimal effect in winter (Leung et al., 2024). The different performance on the visible-band dust optical depth and surface concentrations is not paradoxical, as the observations were made at different locations. The two variables also differ: dust optical depth is a column-integrated variable, whereas surface concentration represents only the bottom model level and depends on the accuracy of simulated vertical dust transport. Because of this difference, another possible explanation for the different behavior in the visible-band dust optical depth versus surface concentration is that the model's vertical mixing of dust aerosols is likely insufficient, as discussed in Section 7.2.1, and has a seasonal cycle that is also not well simulated. Determining the "true" cause requires further investigation, which is beyond the scope of this study.

7.2.3. Dust Size Distribution

Monthly dust size distributions are calculated offline using simulated monthly mass mixing ratios and number concentrations of different aerosol species in each dust mode, the prescribed GSD, and the air temperature and pressure near the atmospheric levels where dust size measurements were taken. Using the calculated monthly

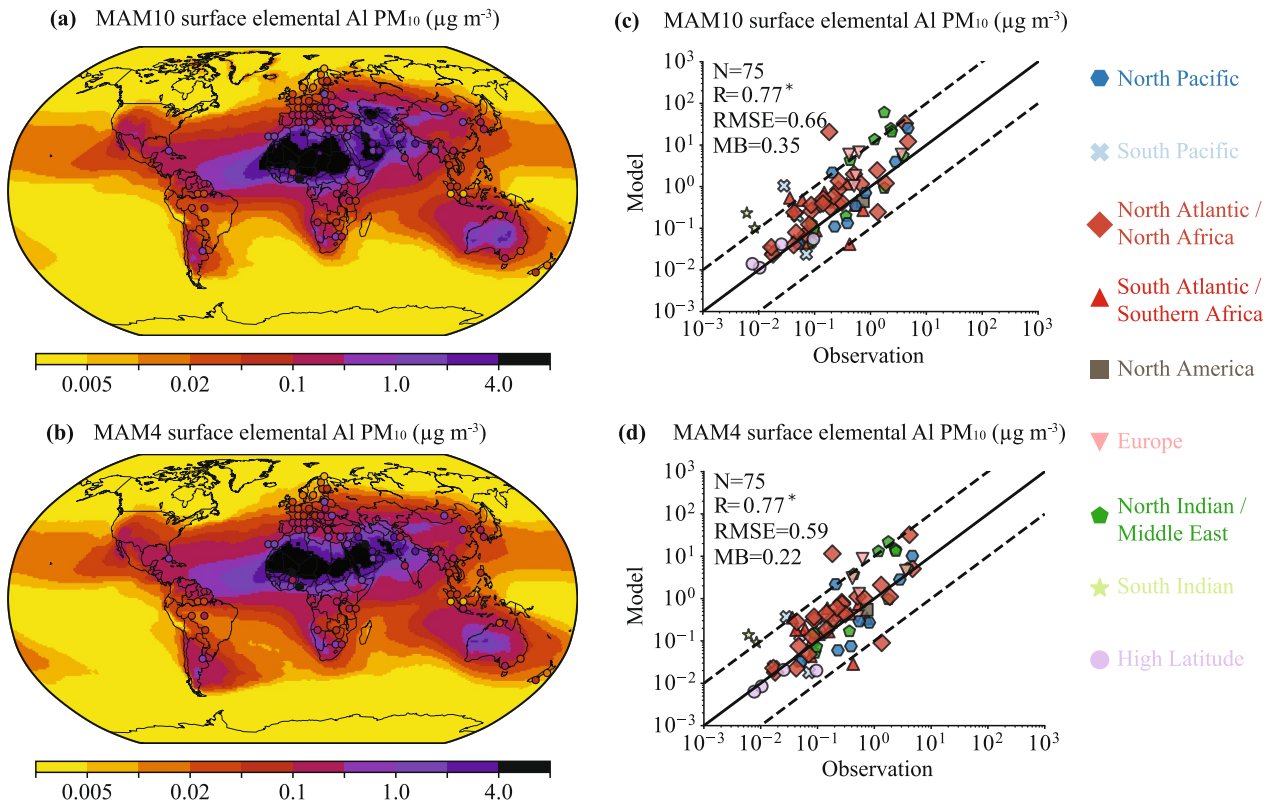

Figure 3. Derived surface elemental aluminum (Al) concentrations based on simulated minerals compared to observations (total number: *N*) previously compiled (Mahowald et al., 2025). Same as Figure 2 but with aerodynamic diameters smaller than 10 μm (Particular Matter: PM_{10}). Panels (a) and (c) correspond to MAM10, and panels (b) and (d) to MAM4. Table S1 in Supporting Information S1 provides the definition of the geographical regions.

values at locations near the measurement sites, the climatological dust size distribution is then derived and compared with observations for the corresponding month.

Three things are worth noting before interpreting the model-observation comparisons. First, there is a non-linear relationship between the dust size distribution and the variables used in the calculations. As a result, using monthly modeled values to compute the monthly dust size distribution may introduce uncertainties, compared to performing the calculations at each model time step and then averaging over a month. Second, the size distribution measurements for dust between 0.40 and 10 μm are more reliable due to the higher data volume within this range (Formenti & Di Biagio, 2024) compared to outside this range, where measuring dust becomes more challenging. Third, in addition to uncertainties introduced during postprocessing (Formenti & Di Biagio, 2024), this data set and the model-observation comparison may face similar shortcomings discussed for the other data sets (Section 6).

Despite any shortcomings in the observations and model-observation comparison, the size settings and reduced settling velocities applied to the last three largest dust modes in MAM10 provide a significantly better representation of observed dust size distributions compared to MAM4, which simulates almost no dust particles larger than 10 μm in diameter (Figure 5). The simulated dust size distributions in MAM10 are within observational uncertainties across most size ranges, except for medium-range transported dust coarser than 50 μm in diameter, which the new mode underestimates (though not significantly), and particles smaller than 0.40 μm, which both models overestimate. MAM10 simulates a clear size dynamic, where the two largest dust modes gradually disappear during transport, while the fine modes remain largely unchanged, which is consistent with observations (Formenti & Di Biagio, 2024). In contrast, MAM4 shows little change in its single coarse mode across varying distances from the source regions.

The new model's performance is improved by incorporating new dust modes that represent super-coarse and giant dust and applying reductions in their gravitational settling velocity: 85% for the giant dust mode and 75% for the

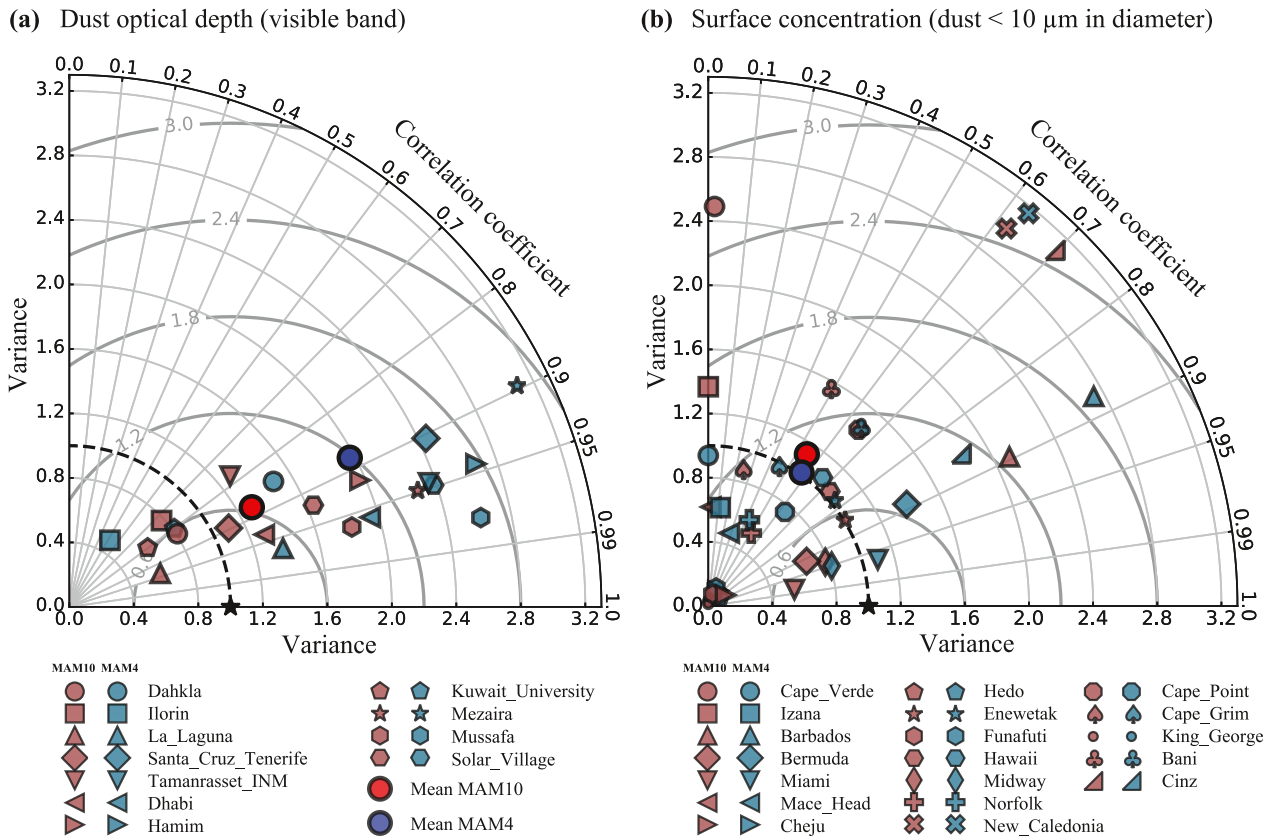

Figure 4. Model-observation comparison of dust aerosol seasonality, defined as the monthly mean climatology. Panel (a) shows results obtained for visible-band dust optical depth, and panel (b) presents results obtained for surface dust concentrations with geometric diameters smaller than 10 μm. Seasonal data compiled by Albani et al. (2014) are used to evaluate the model's performance.

super-coarse dust mode. We also reduce 50% of the simulated gravitational settling velocity for the medium-coarse dust mode. These reductions are generally comparable to the approximately 45%–60% reductions for particles 10–30 μm in the Georgia Institute of Technology-Goddard model (Ginoux, 2003), though lower than the 80% and 90% reductions applied in the Weather Research and Forecasting (WRF) model (Drakaki et al., 2022) and CAM-BAM (Meng et al., 2022), respectively. This reduction amplitude difference could reflect structural (e.g., model resolution) and parametric (e.g., drag coefficients) variations across models.

In MAM10, giant dust particles still likely settle too quickly during medium-range transport, while observations suggest invariant dynamics for dust above 10 μm in diameter, or dust fails to be sufficiently uplifted to reach the measurement altitude. A greater reduction in settling velocity is avoided to prevent overestimating the fraction of dust coarser than 20 μm in diameter over source regions. It is worth noting again the uncertainties in the observations and the model-observation comparison approach, which may complicate the interpretation of the results. For example, the unknown processes (see Section 8) may systematically reduce the settling velocity of super-coarse and giant dust particles only under specific atmospheric conditions, such as episodic periods of enhanced turbulence, that are not uniformly present in space or time. Because modeled climatological mean dust size distributions are compared with measurements from field campaigns that typically last only a few days (Formenti & Di Biagio, 2024) and are therefore more representative of specific events than the models' climatological means, this time mismatch could probably introduce uncertainties in the model-observation comparison, particularly for medium- and long-range transported dust. Nevertheless, the new MAM10 simulates strong temporal variability of dust particles larger than 10 μm in diameter, which is consistent with the sparse, short-term observations (Figure 5b).

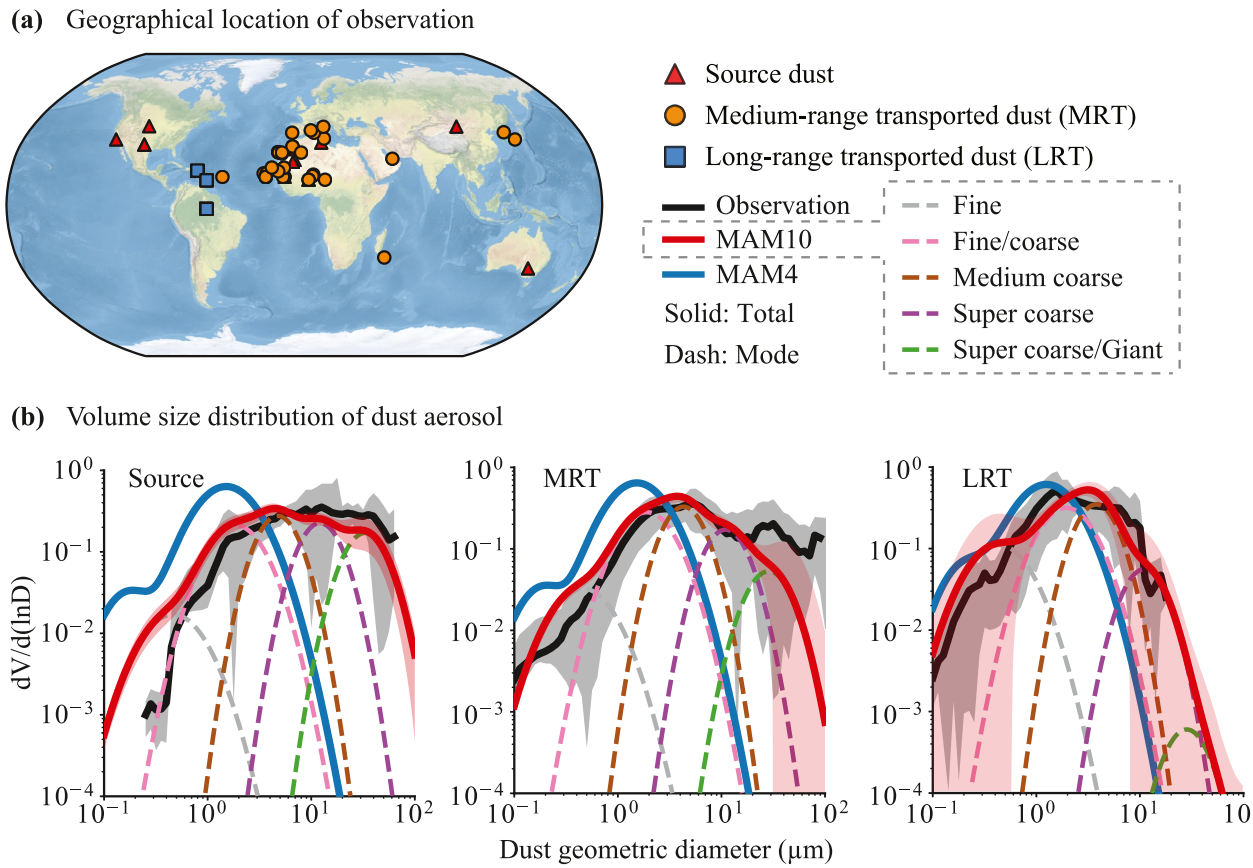

Figure 5. Modeled dust volume size distributions compared to observations previously compiled (Formenti & Di Biagio, 2024). Panel (a) indicates observation locations for the size-resolved data, and panel (b) compares modeled and observed size distributions for dust categorized by transport distance from source regions for MAM10 (red solid lines and dash lines for individual dust modes with shaded 95% confidence intervals across monthly results) and MAM4 (blue solid lines). Model results corresponding to the atmospheric levels, locations, and months of observations (see Formenti & Di Biagio, 2024 for detailed information) are used. Both modeled and observed data are normalized for dust particles across the full-size ranges. The five dust modes in MAM10 correspond to distinct diameter ranges of emitted particles: fine (0.10–1.0 μm), fine/coarse (1.0–5.0 μm), medium coarse (5.0–10 μm), super coarse (10–20 μm), and super coarse/giant (20–70 μm).

7.2.4. Mineral Aerosols

As described in Section 3, the new MAM10 integrates several recent advancements, including: (a) a revised dust aerosol size distribution, (b) an extended brittle fragmentation theory that enables the emission of super-coarse and giant dust particles, (c) an improved EMIT-derived soil mineral atlas, and (d) modified iron oxide content in the three largest dust size modes through updates to the EMIT soil mineral atlas. This study does not attempt a systematic comparison between simulations using the EMIT and pre-EMIT soil mineral atlases, which will be the focus of a forthcoming publication. Nor do we isolate the contribution of each individual development. Instead, our focus is on evaluating the overall performance of the new model, incorporating these combined developments, in reproducing observed mineral fractions in surface concentrations, dry deposition, and total deposition.

Simulations conducted with and without these modifications exhibit similar spatial distributions of mineral mass fractions. However, the combined developments increase the abundance of kaolinite relative to the other minerals (Figure S4 in Supporting Information S1), primarily at the expense of smectite (Figure S4 in Supporting Information S1) and quartz (Figure S5 in Supporting Information S1), as well as iron oxides (Figure 6) and gypsum (Figure S6 in Supporting Information S1), both at the global scale and across the majority of grid cells.

A direct comparison between the new and old models using observed mineral mass fractions is not feasible, as the metrics presented in the paired subpanels of Figure 7 and Figure S7 in Supporting Information S1 correspond to different particle size categories and numbers of observation points (Section 6). Despite this limitation, the new

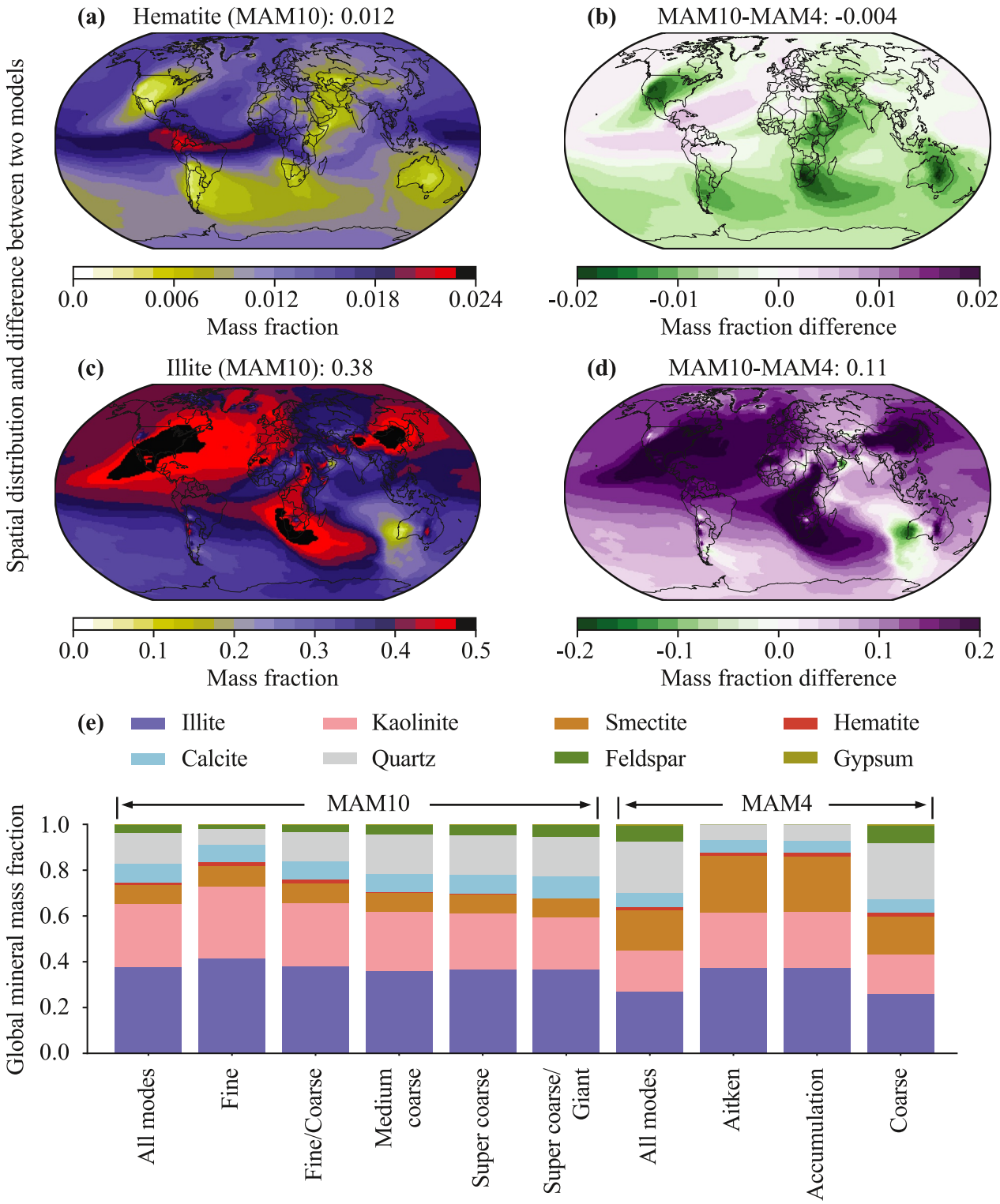

Figure 6. Simulated mineral mass fractions. Panels (a)–(d) show the spatial distribution of simulated hematite and illite, as well as the differences between MAM10 and MAM4 (b and d for hematite and illite, respectively). Panel (e) presents the global mean mass fractions of simulated minerals by MAM10 and MAM4 in different size mode ranges.

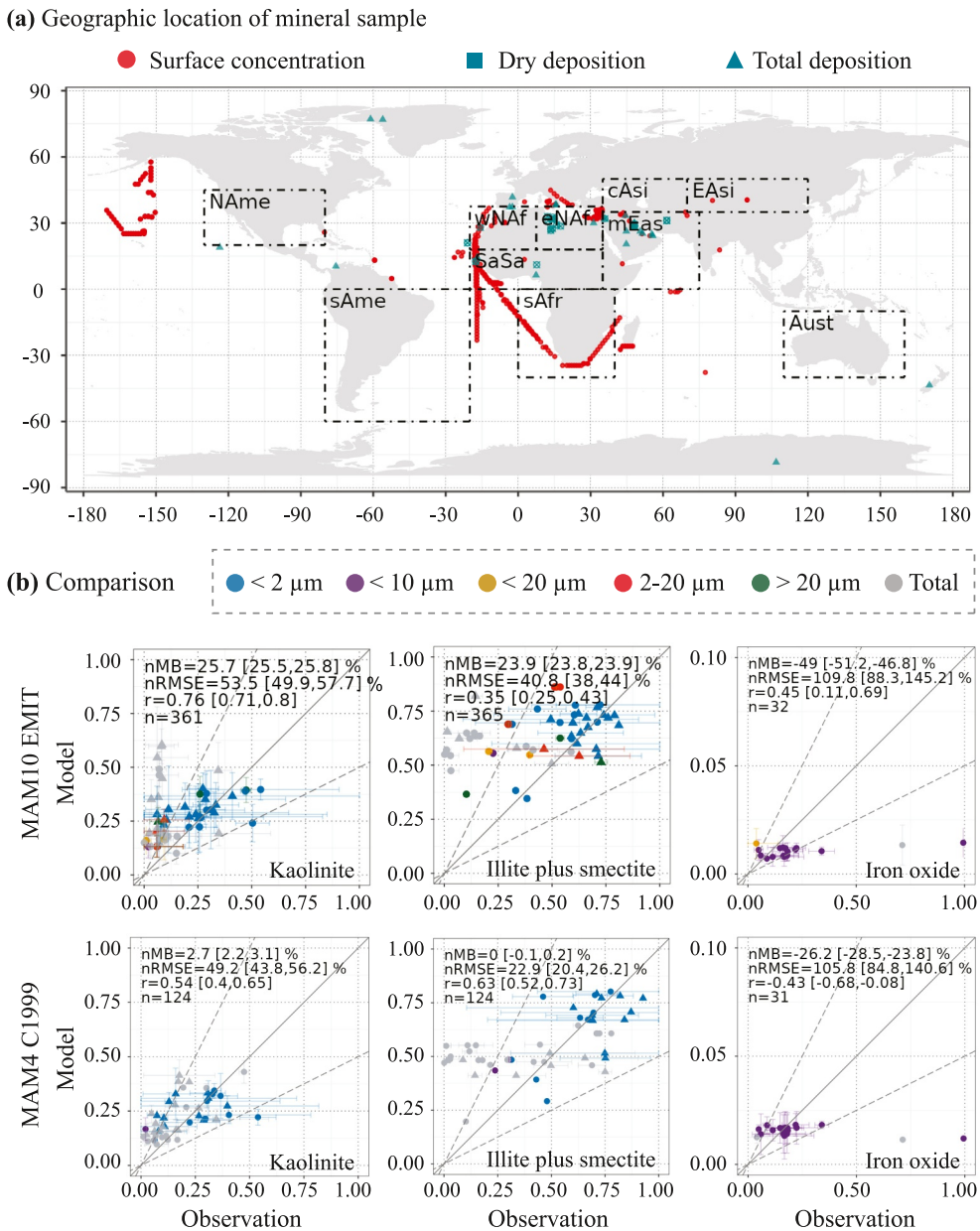

Figure 7. Mineral sample locations and model-simulated mineral fractions in surface concentrations or deposition, compared to previously compiled observations (total number: *n*) (Perlwitz et al., 2015a, 2015b) using the approach of Gonçalves Ageitos et al. (2023). (a) Mineral sample locations categorized by geophysical zones, obtained from surface concentrations (red circles), dry deposition (green squares), or total deposition (green triangles). (b) Model-observation comparisons for kaolinite, smectite, and iron oxides across different size (geometric diameter) segments: top panels for MAM10 with the EMIT soil atlas and bottom panels for MAM4 with the Claquin et al. (1999) soil atlas (C1999). Model performance is evaluated using normalized mean bias (nMB; in percentage), normalized root mean square error (nRMSE; in percentage), and size and spatial correlation (*r*), based on different sample sizes (*n*: number of observational samples used in each plot). See Figure S7 in Supporting Information S1 for the other minerals.

model successfully simulates mineral fractions in dust aerosol particles larger than 10 or 20 μm in diameter, which are not represented in the old model. The extension of mineral size representation alone marks a substantial advancement of the new model over the old one. The existing discrepancies between the modeled and observed minerals do not necessarily reflect limitations in the EMIT surface mineralogy retrievals (see Section 8).

Overall, the new model shows improved capability but still faces challenges in reproducing both the observed magnitude and spatial variability of mineral mass fractions (Figure 7 and Figure S7 in Supporting Information S1). It captures the mass fraction of kaolinite, the combined fraction of illite and smectite (Figure 7), and the combined fraction of quartz, feldspar, and calcite (Figure S7 in Supporting Information S1) within a factor of two at many sites and across multiple size categories. Furthermore, it reproduces the observed spatial distribution of several minerals, including iron oxides with a moderate correlation of 0.45 with measured mass fractions (Figure 7).

Limited observations at sparse locations also indicate size-dependent variations in aerosol mineral composition. For example, the mass fraction of iron oxides tends to decrease with increasing particle size (Kandler et al., 2009; Panta et al., 2023). This trend is captured, to some extent, by the combined modifications (Figure 6e). MAM10 simulates highly uncertain mass fractions of iron oxides in the last two largest dust modes, due to the lack of robust observational constraints on the abundance of iron oxides in super-coarse and giant dust particles. While some studies report almost zero iron oxides in giant dust particles (Kandler et al., 2009; Panta et al., 2023), this reflects an underestimation by their electron microscopy-based approaches, which identify iron oxides in isolated particles but not in inclusions, rather than their actual absence.

7.3. Improved Representation of Size-Resolved Dust Quantities

Dust aerosols of different sizes/modes exhibit varying physical properties, meaning the modeled dust quantities and their distribution among modes are sensitive to changes in size and mode number. Figure 8a addresses how the new model improves the global relative distribution of dust quantities across modes, including the visible-band optical depth, deposition, loadings, and $PM_{2.5}$, compared to MAM4.

In MAM4, a single coarse mode constitutes 80% (Figure 8a) of the total global visible-band dust optical depth, which fails to capture the diverse scattering and absorption behaviors of dust particles of different sizes. The increased number of dust modes in MAM10 addresses this limitation by distributing 70% of the global dust optical depth across the first two smallest dust modes (fine and fine/coarse), with the fine/coarse mode being the primary contributor (50%; Figure 8a). Among the medium-coarse, super-coarse, and super-coarse/giant dust modes, the dust optical depth is more evenly distributed, with each mode contributing minimally. This reduced contribution primarily arises from lower visible-band mass or volume extinction efficiencies and the preferential removal of coarser dust particles by size-dependent aerosol removal mechanisms, such as gravitational settling.

When tuning the model to match the well-constrained global visible-band dust optical depth of approximately 0.030, we adjust the total emitted dust mass to match this total dust optical depth value. Because the mass extinction efficiency of fine dust peaks at visible wavelengths and a substantial portion of dust mass resides in the accumulation/fine and fine/coarse modes, visible-band dust optical depth provides a relatively strong constraint on dust particles within these size ranges. In contrast, this constraint weakens for coarser particles, whose contribution to visible-band dust optical depth is limited, while the observational global dust optical depth is available in the visible band. As a result, tuning based solely on visible-band dust optical depth offers limited leverage on super-coarse and giant dust emissions. To overcome this limitation, alternative constraints, such as satellite-derived infrared-band dust optical depth, which is more sensitive to particles larger than 10 μm in diameter, or retrievals of dust effective diameter, are promising. However, their utility is currently limited by sparse observational coverage and the reliance on a single coarse mode in the retrieval process (Zheng et al., 2022).

In terms of deposition, contributions from differently sized dust modes vary substantially (Figure 8a). In MAM4, the single coarse mode used to simulate dust in the 1.0–10 μm diameter range accounts for 99% of total global dust deposition. In contrast, MAM10 reduces this contribution to 30% by simulating dust in this size range using the fine/coarse and medium-coarse modes. Super-coarse/Giant dust dominates total deposition in MAM10, contributing 40% to the global deposition budget, while fine-mode dust contributes 1.0%, similar to that in MAM4.

The improved representation of dust through additional modes is also evident in the modeled $PM_{2.5}$ at the bottom model level. In MAM10, $PM_{2.5}$ is represented exclusively by fine dust modes (fine and fine/coarse), and the contributions of the three largest dust modes to $PM_{2.5}$ are negligible, while the single coarse mode in MAM4 contributes about 45% of $PM_{2.5}$. Consequently, in MAM4 any attempt to increase coarse-mode aerosols also increases $PM_{2.5}$ aerosols, which limits the ability of the model to separately simulate fine and coarse mode aerosols.

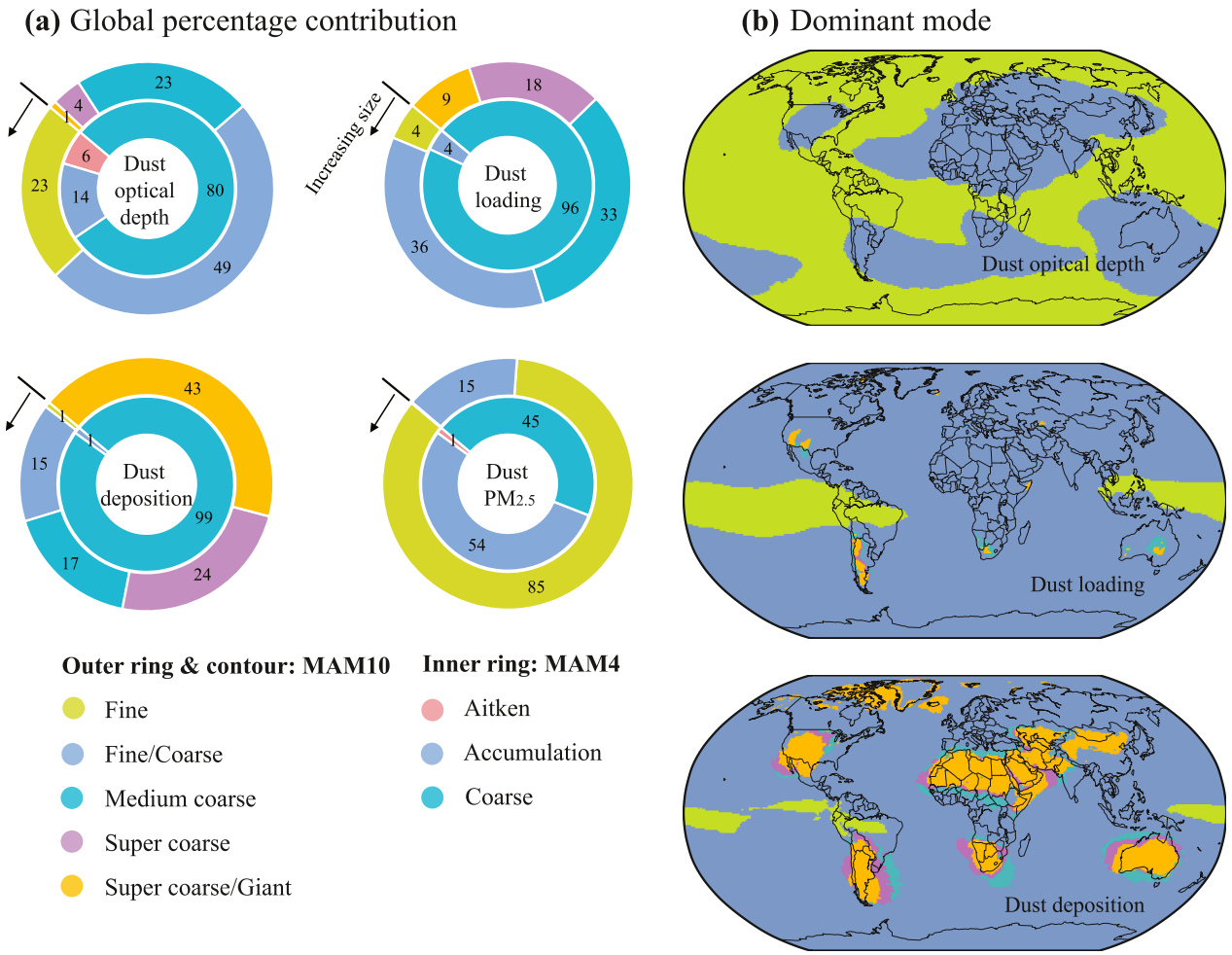

Figure 8. Simulated percentage contributions of individual dust modes to various dust quantities (panel a; MAM10: outer ring; MAM4: inner ring) and spatial distribution of the dominant dust mode in MAM10 (panel b). The dominant mode is the dust mode that contributes the most to a given dust quantity among the five dust modes in MAM10. The dust quantities include: (1) visible-band dust optical depth (top-left rings in panel a and top map in panel b), (2) dust loading (top-right rings in panel a and middle map in panel b), (3) total (dry + wet) dust deposition (bottom-left rings in panel a and bottom map in panel b), and (4) surface particular matter concentrations (bottom-right rings in panel a) with aerodynamic diameters smaller than 2.5 μm ($PM_{2.5}$). The five dust modes in MAM10 cover geometric diameter ranges of 0.10–1.0 (fine), 1.0–5.0 (fine/coarse), 5.0–10 (medium coarse), 10–20 (super coarse), and 20–70 μm (super coarse/giant), respectively, for emitted particles. In comparison, the three dust modes, Aitken, accumulation, and coarse, in MAM4 cover geometric diameter ranges of 0.010–0.10, 0.10–1.0, 1.0–10 μm, respectively.

Spatially, the distinct physical properties of different dust modes and the distribution of dust mass or number fluxes over them highlight their distinct roles in influencing the visible-band dust optical depth, loadings, and deposition across regions (Figure 8b). Specifically, Figure 8b suggests the following three key findings.

First, the fine mode along with the fine/coarse mode dominates visible-band dust optical depth everywhere: in the tropics along the Intertropical Convergence Zone (ITCZ), and in high-latitude regions controlled by the fine mode, and the other regions dominated by the fine/coarse mode. However, coarser dust modes (larger than 5.0 μm in diameter) can contribute over 30% near or over source regions (Figure S8 in Supporting Information S1). Therefore, an inappropriate representation of dust aerosols larger than 5.0 μm in diameter may lead to the misestimation of finer dust emission, given the tuning process used to achieve a global visible-band dust optical depth of 0.030. For example, neglecting the contribution of coarser modes to the global dust optical depth could result in excessive emissions of finer dust from source regions to compensate for the missing contribution from coarser particles.

Second, the fine/coarse mode dominates the dust loadings in most grid cells (Figure 8b) due to its longer atmospheric lifetime compared to coarser modes and its higher emission rates relative to dust in the fine mode. The relatively large contribution of medium-coarse/super-coarse/giant dust modes over marginal deserts, compared

with major deserts, may reflect a stronger influence of local emissions and a weaker contribution from transported dust, which is preferentially depleted in coarse particles during transport. In contrast, the dust size distribution over major deserts includes the impact of local emissions but also particles from upwind sources that have been depleted at large diameters.

Third, the two smallest dust modes (fine and fine/coarse) also dominate dust deposition in remote regions and along the ITCZ, whereas the super-coarse/giant dust mode's dominant influence remains confined to areas near dust sources due to its large size and short atmospheric lifetime. This spatial pattern (Figure 8b) underscores the critical role of the two smallest dust modes in transporting nutrients such as iron and phosphorus to ecosystems like the Amazon rainforest and the central Pacific. Their contributions exceed those of larger modes, except in ocean regions proximal to major dust sources (e.g., the western African coast, South America, southeastern Africa, and the southeastern United States), where local deposition is dominated by coarser particles. The two smallest dust modes actually dominate most dust quantities, except for total global deposition, which is primarily simulated by the super-coarse/giant dust mode.

7.4. Role of Dust Particles Larger Than 10 Microns in Diameter

Our model results suggest that dust particles larger than 10 μm in diameter are an important component of dust aerosols and should be included in models to estimate global and regional (source-containing) dust budgets, consistent with findings from a previous study using an alternative model (Adebiyi et al., 2023). Globally, these particles contribute 70% of the total deposition flux and 30% of the total atmospheric loading in MAM10 (Figure 8a), which is slightly lower than a previous estimate of 35% (Adebiyi et al., 2023). While most of these particles (diameters larger than 10 μm) remain near dust source regions, such as the Sahara and the Sahel, a considerable amount of dust mass can be transported over long distances, as observed in various measurements (Prospero et al., 1970; Ryder et al., 2013, 2018, 2019; Weinzierl et al., 2009, 2017) and previously simulated (Adebiyi et al., 2023). These transported particles larger than 10 μm in diameter can still deposit onto remote ecosystems, including ocean basins, the Amazon Rainforest, Greenland, Antarctica, and the Tibetan Plateau, where they supply essential micro- and macronutrients.

Our calculations reveal a substantial increase in dust deposition across different regions when super-coarse and giant dust particles are included, which is also revealed by a previous study (Adebiyi et al., 2023), along with the improved representation of particles in the 5.0–10 μm size range (Figure 9). Therefore, the inclusion of such super-coarse and giant particles highlights the potential for a great upward revision of previously estimated dust budgets (Kok et al., 2023) and probably their climate impacts, particularly through altering the land and ocean biogeochemistry, despite a disproportionally low impact of this fraction of dust on the direct radiative effect relative to their contribution to the dust budget. This increase, however, is strongly regionally dependent, with the largest enhancements confined to major dust source regions (Figure 8b and Figure S8 in Supporting Information S1). The impacts of this dust fraction will be quantified in our future papers.

Given the limited availability of high-quality observations, the new model likely underestimates dust deposition in the Southern Ocean, with values an order of magnitude lower than previous estimates (Kok et al., 2023), even without accounting for dust coarser than 20 μm in diameter (2.0 vs. 25 Tg year^{-1}). The separation of sea salt from dust aerosols was intended to mitigate the excessive wet removal of dust observed in MAM4, particularly in regions downwind of South American sources, such as the Patagonian Desert. The effect, however, is weaker than anticipated.

Although the global contribution of dust particles larger than 10 μm in diameter to the total visible-band dust optical depth is small, their regional impact can be considerable. For example, campaign measurements over the Sahara Desert indicate a 40% contribution to the total dust optical depth at 0.55 μm (Ryder et al., 2018), which is similarly simulated here (Figure S8 in Supporting Information S1) and overall consistent with another study (Adebiyi et al., 2023). This suggests that, although excluding dust larger than 10 μm in diameter may not considerably affect the global visible-band dust optical depth, it could bias estimates of the finer dust emission toward higher values, especially near source regions such as in the Sahara Desert, to compensate for the missing contribution of dust larger than 10 μm in diameter, given that the model is tuned to a global visible-band dust optical depth of 0.030. Since fine-sized dust has a longer atmospheric lifetime and tends to scatter solar radiation more than it absorbs, this bias could result in three key outcomes: (a) increased transport of dust away from source

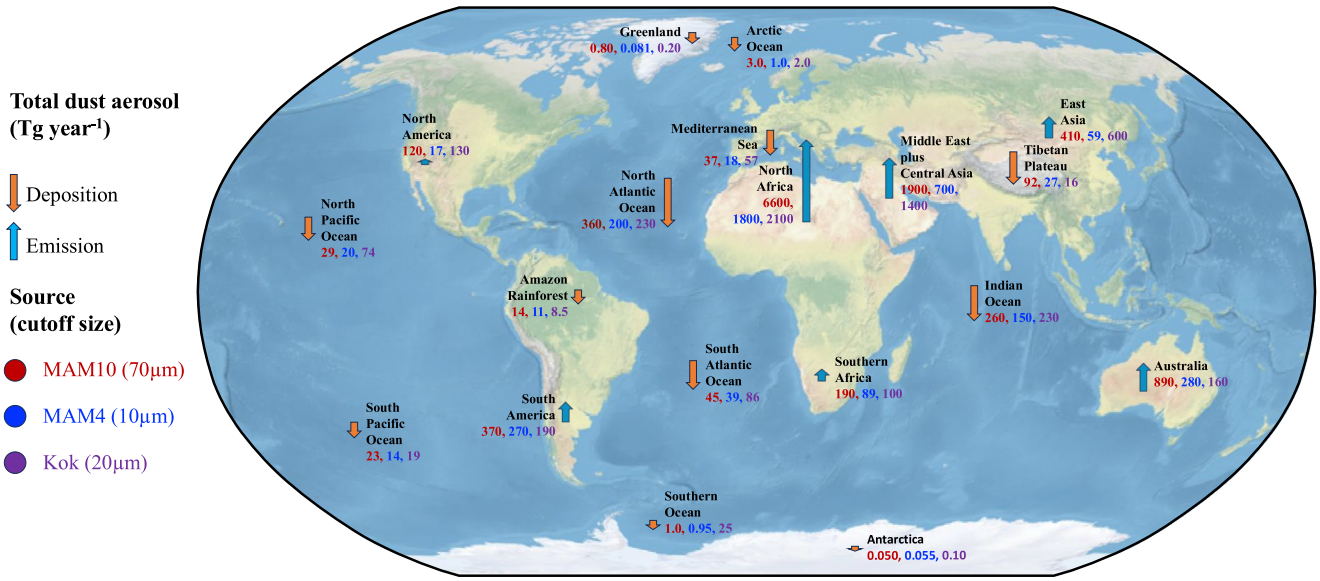

Figure 9. Regional dust emission and deposition budgets (Tg year^{-1}). Upward blue arrows represent dust emissions, and downward orange arrows indicate total (dry + wet) dust deposition. Numbers in red, blue, and purple correspond to results from MAM10 (dust geometric diameters smaller than 70 μm at emission), MAM4 (dust geometric diameters smaller than 10 μm at emission), and the best estimates (geometric diameters smaller than 20 μm) from Kok et al. (2023), which integrate observations with multi-model simulations. Arrows indicate dust emissions or deposition. Upward arrows represent dust emissions, and downward arrows represent dust deposition. The arrows are used solely to illustrate the direction and presence of emission and deposition and are only qualitatively scaled to represent their relative magnitudes. The marine geophysical definitions follow the shapefiles available at https://marineregions.org/, while the continental definitions follow Python's built-in geophysical files. The Amazon forest is included as a key terrestrial receptor where long-range dust deposition supplies essential nutrients to ecosystems and biogeochemistry. The Tibetan Plateau is also highlighted as a sensitive high-altitude receptor where dust deposition can have disproportionate cryospheric and hydrological impacts; other land regions are omitted to emphasize long-range transport pathways and representative receptor regions.

regions; (b) enhanced direct radiative cooling effect everywhere; and (c) overestimation of $PM_{2.5}$ levels over source regions, such as Sahel and Sahara deserts.

8. Further Discussion and Conclusions

This study addresses two previously unresolved issues in CESM2: (a) the absence of dust particles larger than 10 μm in diameter, whose substantial presence is indicated by observations, and (b) the underrepresentation of dust mass and particle number between 1.0 and 10 μm, which relies on a single mode that unrealistically dominates most dust quantities. These goals are achieved through the addition of modes representing larger particle diameters within the new mineral-resolved aerosol framework, MAM10. Importantly, the results of this study cannot be fully reproduced by prescribing a new broader dust size distribution within the single coarse mode (Table 1) used by previous CESM configurations. The limitation addressed here is structural: when dust is represented by a single coarse mode, size-dependent processes such as gravitational settling, deposition, and radiative interactions act at a single mode-mean particle size, preventing the simultaneous representation of very large particles and smaller coarse dust. By explicitly resolving coarse and giant dust with separate prognostic modes, the framework introduced here enables an internally consistent coupling between emission, transport, deposition, and radiation at distinct sizes that cannot be achieved through the currently prescribed coarse-mode size distribution in the MAM4 configuration. Moreover, because aerosol modes in CESM are internally mixed and shared by multiple species, prescribing a broader dust size distribution within the existing framework would unavoidably distort the size-dependent behavior of non-dust aerosols, whereas the expanded modal structure introduced here allows dust-specific size resolution without compromising other aerosol components.

The new model also simulates more comprehensive dust emission physics, building upon previous work (Ke et al., 2022; Leung et al., 2024; Li et al., 2022b; X. Liu et al., 2012), and uses a new EMIT atlas of surface soil mineralogy (P. G. Brodrick, Green, et al., 2023; Green et al., 2020) that is based upon a considerably larger number of measurements in dust source regions compared to pre-EMIT soil atlases (Claquin et al., 1999; Journet et al., 2014). A surface erodibility constraint is also imposed using the GUM data set (Börker et al., 2018).

The model results compared to observations at varying distances from sources (Formenti & Di Biagio, 2024) indicate an improved representation of dust size distribution (Figure 5), including particle diameters larger than 10 and up to 70 μm at emission. This improvement is mainly due to the introduction of new modes and a reduction in the modeled gravitational settling velocity of dust particles in the last three dust modes (corresponding to the largest diameters), consistent with previous studies (Drakaki et al., 2022; Ginoux, 2003; Meng et al., 2022), whereas the impact of the updated visible-band mass extinction efficiency associated with EMIT-derived iron oxides is negligible. With such improvement, the updated model maintains the overall dust cycle accuracy of MAM4 for particles under 10 or 2.5 μm in diameter when compared with observations for visible-band dust optical depth (Figure 1), surface elemental aluminum concentrations (a proxy for dust aerosols) (Figures 2 and 3), and total dust deposition (Figure 1).

The new MAM10 also more realistically simulates the seasonal variation of visible-band dust optical depth (Figure 4) and the distribution of dust across size ranges (Figure 8), addressing a key limitation in MAM4. In MAM4, a realistic $PM_{2.5}$ results in an unrealistic mass of dust at larger diameters due to the limitation of a single coarse mode representing both $PM_{2.5}$ and coarser particles. By introducing additional modes at larger diameters, MAM10 allows the coarser dust fraction to vary independently of the fine fraction, which now more appropriately dominates $PM_{2.5}$.

Although our results regarding dust larger than 10 μm in diameter are subject to large uncertainty (as discussed below), they emphasize the importance of simulating a fuller dust size distribution than what was typically done in previous studies (Ginoux et al., 2001; Li et al., 2022b; Zender, Bian, & Newman, 2003) for accurately representing the dust cycle and its climate effects. Dust particles coarser than 10 or 20 μm in diameter need to be included in both regional and global models for two reasons.

First, they substantially influence the simulated dust mass (Table 4 and Figure 9) (Adebiyi et al., 2023). Including these particles will increase previous estimates of dust source emission and downwind deposition budgets, and the magnitude of the longwave dust direct radiative effect (Albani et al., 2014; Kok, et al., 2021a, 2021b; Kok et al., 2023; Li et al., 2022b).

What is more important is that, even though large dust particles do not affect the visible-band dust optical depth in proportion to their impact on the deposition flux, dust particles coarser than 10 or 20 μm in diameter still can constitute a considerable fraction of the visible-band dust optical depth regionally due to their large mass fraction near source regions (Figure S8 in Supporting Information S1). The common practice of tuning models to match a global visible-band dust optical depth target (e.g., 0.030) while omitting dust larger than 10 μm in diameter can introduce compensating biases, particularly in dust source regions. Specifically, models excluding larger particles may overestimate the emission of fine dust to reproduce the observed visible-band dust optical depth, leading to an undue enhancement of long-range dust transport, direct radiative cooling, and $PM_{2.5}$ concentrations over regions like the Sahel and Sahara. These biases highlight the importance of explicitly representing dust larger than 10 μm in diameter, not only to refine dust source and sink estimates but also to improve assessments of dust climate impacts through dust-radiation interactions (Kok et al., 2017) and effects on land and ocean biogeochemistry (Jickells et al., 2005; Mahowald, 2011; Mahowald et al., 2010, 2018; Mccutcheon et al., 2021; Meskhidze et al., 2005).

Regarding the dust mineral composition, while a systematic comparison of simulated mineralogy using EMIT and pre-EMIT soil mineral atlases is reserved for a forthcoming study, this study highlights the effects of key model developments on simulated mineral fractions and their consistency with observations. Specifically, the new MAM10 extends the capabilities of MAM4 by enabling the simulation of minerals in dust particles larger than 10 or 20 μm in diameter, although challenges remain in reproducing observed mineral mass fractions across different size categories (Figure 7 and Figure S7 in Supporting Information S1). This extension, compared to previous studies, provides insights into the climate impacts of dust, which remain highly uncertain, especially when considering dust aerosol mineralogy (Li et al., 2021) and size distribution (Kok et al., 2017; Mahowald et al., 2014). The revised assessment of these impacts, along with a detailed evaluation of the vertical dust distribution and mineral composition, will be discussed in our forthcoming paper(s) (e.g., Li, Mahowald, Obiso, et al., 2025).

The remaining discrepancies between modeled and observed dust mineral aerosols may stem from deficiencies in the EMIT soil mineral atlas (e.g., the relatively uncertain retrieval of the mineral mass fraction in the soil, given

identification of the mineral, or else misidentification of certain nano-hematite-nano-goethite mixtures as jarosite, a mineral with optical properties that are distinct from those of hematite and goethite) and from the representations of iron oxides in the model (e.g., the omission of nano-iron oxides as a mineral component). Furthermore, the EMIT instrument cannot directly detect quartz and feldspar, as these minerals lack diagnostic Visible to Shortwave Infrared (VSWIR) absorption features. Instead, the presence of these minerals is inferred in part from existing soil mineralogy atlases, which carry substantial uncertainties in their abundances in clay- and silt-sized categories. All these limitations, whose significance may depend on particle size, also hinder models from accurately capturing the size dependence of key mineral components (e.g., iron oxides and K-feldspar), and, consequently, from reliably quantifying dust's climate impacts. Additional sources of error include inaccuracies in the dust size distribution, emission, transport, and deposition processes; observational uncertainties (including the limited availability of mineralogical composition measurements for dust aerosols), and the model-observation comparison methodology. Therefore, the model biases and discrepancies do not necessarily provide a complete reflection of the accuracy of the soil mineralogical characterization in the EMIT atlas.

Despite the advancements, several challenges remain that hinder the model's ability to accurately simulate the dust cycle with a physical basis, particularly in reproducing the dust size distribution.

First, there is a lack of precise measurements of the size distribution of mineral dust in the size range larger than 20 μm in diameter, especially in source regions (Formenti & Di Biagio, 2024), limiting the ability to constrain emission and atmospheric abundance of dust (mineral) aerosols at large diameters (primarily applied to quartz, feldspar and possibly carbonates that dominate the mineral fractions measured at these diameters). This scarcity stems from various factors, including a historical underestimation of the importance of large dust particles, instrumental challenges for airborne measurements (e.g., low sampling efficiencies of instrument inlets) (Adebiyi et al., 2023), and the rarity of field campaigns equipped to capture the full dust size distribution, given that instruments such as light optical aerosol counters or multiple aerosol spectrometers (Ryder et al., 2013, 2018, 2019; Weinzierl et al., 2009, 2017) only detect subsets of the dust size distribution. Consequently, our global estimates of total dust and the contributions of particles larger than 10 or 20 μm in diameter remain highly uncertain.

A second challenge involves simulating dust particles larger than 5.0 μm in diameter, which may behave differently from finer particles in terms of transport, deposition, and radiative effects. An accurate representation of their transport and deposition could be crucial for quantifying their regional and global impacts. While empirically reducing the gravitational settling velocity of large dust particles, particularly at geometric diameters larger than 20 μm, can achieve certain improvements like those shown here (Figure 5) and in previous studies (Drakaki et al., 2022; Ginoux, 2003; Meng et al., 2022), the physical mechanisms for slowing descent of these particles remain unclear (van der Does et al., 2018), as earlier studies also noticed (Betzer et al., 1988; Mahowald et al., 2005).

Recent findings suggest potential mechanisms for maintaining particles aloft, such as topography (Heisel et al., 2021; Rosenberg et al., 2014), electric forces on charged particles (Toth et al., 2020; van der Does et al., 2018), underrepresented uplift by convection events (combining the other possible mechanisms or multiple uplifts occurring within a long-lived system) (van der Does et al., 2018) or turbulence (radiation- or shear-induced) in the free troposphere (Rodakoviski et al., 2023), horizontal and vertical resolutions of models (Feng et al., 2022) or aerosol splitting processes in models (Wan et al., 2024), and variations in particle shape and orientation (Bagheri & Bonadonna, 2016; Huang et al., 2020; Mallios et al., 2020). Testing these mechanisms is beyond the scope of this study but deserves future investigations. Here, we only approximate the effects by adjusting the gravitational settling velocity for dust particles represented by the last three dust modes corresponding to the largest diameters. However, this adjustment is applied uniformly across regions, ignoring potential spatial and temporal variability.

The third challenge is on the accurate representation of the physical (e.g., optical) and chemical properties of dust particles larger than 20 μm in diameter based on their mineral composition, which affects dust climate impacts. Translating soil composition into aerosol mineralogy is particularly challenging for iron oxides and quartz in giant dust aerosol particles due to the scarcity of measurements and the need for advanced techniques. Dust aerosol particles larger than 20 μm in diameter are difficult to sample and analyze compared to particles smaller than 10 μm in diameter. Uncertainties stemming from the representation of atmospheric processes, such as chemical reactions and cloud processing (Langmann, 2013; Longo et al., 2016; Usher et al., 2003), are also likely limited

for dust particles larger than 20 μm in diameter, because these processes scale primarily with particle number or surface area concentrations, which remain relatively low in this size range even when large particles contribute substantially to the volume or mass size distribution (Figure 5).

Fourth, several factors influencing the modeled dust size distribution, such as the prescribed GSD as a global constant for each mode and the settling velocity for particles larger than 5.0 μm in diameter, remain poorly constrained. Empirical tuning is used in this study to match observed size distributions. While observationally derived GSDs can be prescribed, missing or inaccurate physics, such as mechanisms for maintaining particles aloft, or other unknown errors may have hindered achieving the intended outcomes. Therefore, we adjust dust parameters to match the observed size distribution. This empirical approach is sufficient for specific applications like the estimate of the dust radiative effect at short wavelengths that is central to the EMIT mission, and which depends upon an accurate spatial distribution of dust particles, including large sizes (Li, Mahowald, Obiso, et al., 2025). However, there is still room for refinement of physics-based models of the gravitational settling velocity (Figure 5), which might lead to different results.

Additional approaches to constrain super-coarse and giant dust particles are to evaluate the model with dust optical depth or effective diameter retrieved at thermal wavelengths (Zheng et al., 2022). However, uncertainties in the longwave optical depth retrievals could make this challenging. Sparse observations of effective diameters —limited by assumptions such as mono-modal particle size distributions, the near absence of reliable observations over land (Zheng et al., 2022), and uncertainties in the emitting temperature of dust layers, partly due to substantial variability in the vertical structure of dust plumes from one event to another (Li & Sokolik, 2018)— further complicate this method. Future accurate retrievals of effective diameter could potentially reduce uncertainties in modeling the large dust particle cycle as well (especially diameters larger than 20 μm), in addition to uncertainties in longwave dust radiative effect estimates. These approaches are deferred to future investigations.

Fifth, reproducing the dust cycle across different environments and measurements remains challenging. The complex interactions of factors like surface winds, vegetation, and soil moisture dynamics (Kok et al., 2012; Shao, 2008) govern dust emission, transport, and deposition. Uncertainties in model parameterization that affect these processes further complicate predictions for different dust phases. As a result, like MAM4 (Li et al., 2022b), the new model cannot match the observed dust deposition, visible-band dust optical depth, and surface aluminum elemental PM_{10} concentrations simultaneously (Figures 1 and 3), which has been recognized for more than a decade (Huneeus et al., 2011).

Sixth, dust-cloud interactions (DeMott et al., 2003; Karydis et al., 2011) are not included in the new MAM10 model for particles with diameters larger than 20 μm. Their impact is likely minimal, as cloud effects scale with aerosol number concentrations (Andreae & Rosenfeld, 2008), which are very low for dust larger than 20 μm in diameter. Regionally, however, these interactions may influence the ice-nucleating particle population in areas proximal to dust source regions, where super-coarse/giant dust particles are relatively abundant, such as the eastern tropical Atlantic (Adebiyi et al., 2023). In addition, radiative effects of super-coarse/giant dust on clouds (the semi-direct effect), while potentially non-negligible, remain highly uncertain and warrant further investigation.

Lastly, MAM10 does not account for additional constituents except sulfate that may be internally mixed with dust aerosols, such as soot and primary biological particles (e.g., microorganisms and biological material fragments) (Kellogg & Griffin, 2006; Shinn et al., 2000). The mixing of these species with dust aerosols is excluded from the MAM10 framework presented here. Below, we outline the specific reasons, using sea salt as an example; however, future studies may need to investigate the impact of an alternative treatment, in which dust is internally mixed with these species, on simulations of the dust cycle and its climate effects.

The external mixing of dust with the other species except sulfate is inherited from previous aerosol model versions, MAM7 and MAM9, for simplicity. Here, we advance the model to simulate a fuller and more accurate size distribution of dust aerosols. While MAM4 simulates dust as a mixture with other components, such as sea salt, the mechanisms driving the mixing of dust particles and sea salt remain insufficiently detailed (Andreae et al., 1986; D. Zhang et al., 2005). The mixing state of dust and sea salt also depends on the region. Observations show infrequent internal mixing of African dust with sea salt, particularly during peak dust outbreak seasons across the Atlantic Ocean (Kandler et al., 2007; E. Reid et al., 2003) when the dust plume is elevated. In these scenarios, African dust particles are typically transported above the marine boundary layer (Karyampudi

Acknowledgments
L.L., N.M.M., R.L.M., and R.N.C. received support from the NASA EMIT project. EMIT is supported by the NASA Earth Venture Instrument program under the Earth Science Division of the Science Mission Directorate. L.L. and N.M.M. also acknowledge assistance from the Department of Energy (DOE) under Grant DE-SC0021302, the high-performance computing resources from Derecho provided by National Center for Atmospheric Research (NCAR)'s Computational and Information Systems Laboratory (CISL), sponsored by the National Science Foundation (NSF), and a NASA Interdisciplinary Science (IDS) project under Grant 80NSSC20K1674. C. P.G.P., M.G.A., and V.O. acknowledge funding by the European Research Council under the Horizon 2020 research and innovation program through the ERC Consolidator Grant FRAGMENT under Grant 773051, the AXA Research Fund through the AXA Chair on Sand and Dust Storms at BSC, and the European Union's Horizon 2020 research and innovation program under grant agreement No 821205 (FORCeS). C.P.G.P and V.O. also acknowledge Grant PID2022-140365OB-I and M.G.A. acknowledges Grant PID2022-139362OB-I00, both funded by MICIU/AEI/10.13039/501100011033 and by ERDF, EU. R.L.M. also received support from the NASA Modeling, Analysis, and Prediction Program under Grant NNG14HH42I. J.F.K. acknowledges support from the NSF Directorate for Geosciences under Grants 1856389 and 2151093. P.F. and C.D.B. received support from the DustClim project, which is part of ERA4CS, an ERA-NET project initiated by JPI Climate and funded by FORMAS (SE), DLR (DE), BMWFW (AT), IFD (DK), MINECO (ES), and ANR (FR) with co-funding from the European Union's Horizon program under Grant 690462. P.F. and C.D.B. also received support from the French national program LEFE/INSU (Les Enveloppes Fluides et l'Environnement/Institut National des Sciences de l'Univers) and by the OSU-EFLUVE (Observatoire des Sciences de l'Univers-Enveloppes Fluides de la Ville à l'Exobiologie) through dedicated research funding to the RED-DUST project, and the European Union's Horizon 2020 research and innovation program through the EUROCHAMP-2020 Infrastructure Activity under Grant 730997. C.D.B. was supported by the Centre National des Etudes Spatiales (CNES) and by the CNRS via the Labex L-IPSL, which is funded by the ANR under Grant ANR-10-LABX-0018. D.M.L. acknowledges support from the NSF NCAR Advanced Study Program (ASP) Postdoctoral Fellowship and from the Quadrature Climate Foundation (QCF) under Grant 01-21-000349. A portion of this research was performed at the Jet Propulsion Laboratory (JPL),

et al., 1999) and dust layers remain distinct from it (J. S. Reid et al., 2002), resulting in frequently low sea salt mass fractions (less than 10%) in dust plumes (Chiapello et al., 1999). In contrast, East Asian dust transported eastward shows higher degrees of internal mixing with soluble salts (Niimura et al., 1998), including sea salt, ranging from 18% to 42% by volume (Osada, 2013). Over 60% of dust particles collected at Japanese islands, after several hours of transport through marine air, were found internally mixed with sea salt (Niimura et al., 1998; Okada et al., 1990; D. Zhang et al., 2003). Based upon these findings, the separation of dust and sea salt in MAM10 may not be a good assumption for East Asian dust aerosols, potentially biasing estimates of their wet removal rates and climate effects. Moreover, observations on the mixing state of dust with sea salt, especially in the Southern Ocean, are far more limited. For the mixing of primary biological particles with dust aerosols, some attempts exist (Adachi et al., 2020; Brodsky et al., 2023), but the results remain preliminary.

Beyond addressing current limitations, the new model developed in this study allows a more complete and accurate representation of the dust climate impacts than previous CAM versions. It complements existing models (Di Biagio et al., 2020; Ke et al., 2022; Wang et al., 2024) in quantifying the role of super-coarse and giant dust particles in dust-radiation interactions and their influence on modeling trace metal deposition, which is critical for terrestrial and ocean biogeochemistry (Brodsky et al., 2023; Lu et al., 2024; Mahowald et al., 2018; Wong et al., 2021).

The modeling framework developed here not only improves the representation of large dust particles but could also be used to simulate other aerosols with broad size distributions, such as volcanic ash, whose size often exceeds 10 μm in diameter (Brown et al., 2012).

Recognizing all the unresolved issues, future research should pursue more comprehensive analyses that incorporate a broader range of species present in dust aerosols and adopt more physically based modeling approaches to simulate large dust aerosols under observational constraints. Such advances will help improve the accuracy of regional and global climate assessments and enhance our understanding of aerosol composition and its role in the Earth-Human-Climate system.

Conflict of Interest

The authors declare no conflicts of interest relevant to this study.

Data Availability Statement

The core component of the CAM6-MAM4 and observations (AERONET dust aerosol optical depth, surface concentrations, and deposition fluxes) are available from Li et al. (2022a). The MAM10 code is available from Li (2025). The dust-related quantities simulated by MAM10 are available from Li (2026). The EMIT soil mineralogy data is publicly available from P. Brodrick et al. (2025). The elemental aluminum data is available from Mahowald, Li, Vira, et al. (2024). Detailed documentation of the observed mineral fractions can be found in previous studies (Gonçalves Ageitos et al., 2023; Perlwitz et al., 2015a, 2015b). The database of dust size distribution is available from Formenti and Di Biagio (2023a, 2023b, 2023c).

References

Adachi, K., Oshima, N., Gong, Z., De Sá, S., Bateman, A. P., Martin, S. T., et al. (2020). Mixing states of Amazon basin aerosol particles transported over long distances using transmission electron microscopy. *Atmospheric Chemistry and Physics*, *20*(20), 11923–11939. https://doi.org/10.5194/acp-20-11923-2020

Adebiyi, A. A., Kok, J. F., Murray, B. J., Ryder, C. L., Stuut, J.-B. W., Kahn, R. A., et al. (2023). A review of coarse mineral dust in the Earth system. *Aeolian Research*, *60*, 100849. https://doi.org/10.1016/j.aeolia.2022.100849

Adebiyi, A. A., & Kok, J. F. (2020). Climate models miss most of the coarse dust in the atmosphere. *Science Advances*, *6*(15), 1–10. https://doi.org/10.1126/sciadv.aaz9507

Adebiyi, A. A., Kok, J. F., Wang, Y., Ito, A., Ridley, D., Nabat, P., & Zhao, C. (2020). Dust constraints from joint observational-modelling-experimental analysis (DustCOMM): Comparison with measurements and model simulations. *Atmospheric Chemistry and Physics*, 829–863. https://doi.org/10.5194/acp-2019-484

Albani, S., Mahowald, N. M., Perry, A. T., Scanza, R. A., Zender, C. S., Heavens, N. G., et al. (2014). Improved dust representation in the Community Atmosphere Model. *Journal of Advances in Modeling Earth Systems*, *6*(3), 541–570. https://doi.org/10.1002/2013MS000279

Andreae, M. O., Charlson, R. J., Bruynseels, F., Storms, H., Van Grieken, R., & Maenhaut, W. (1986). Internal mixture of sea salt, silicates, and excess sulfate in marine aerosols. *Science*, *232*(4758), 1620–1623. https://doi.org/10.1126/science.232.4758.1620

Andreae, M. O., & Rosenfeld, D. (2008). Aerosol-cloud-precipitation interactions. Part 1. The nature and sources of cloud-active aerosols. *Earth-Science Reviews*, *89*(1–2), 13–41. https://doi.org/10.1016/j.earscirev.2008.03.001

California Institute of Technology, under a contract with NASA. We thank Raymond F. Kokaly, Gregg A. Swayze, Francisco Ochoa, Abigail Keebler, and Bethany L. Ehlmann for their contributions to the generation of the EMIT soil mineral atlas, and John Dunne for conducting the GFDL internal review.

Bagheri, G., & Bonadonna, C. (2016). On the drag of freely falling non-spherical particles. *Powder Technology*, *301*, 526–544. https://doi.org/10.1016/j.powtec.2016.06.015

Bagnold, R. A. (1941). *The physics of blown sand and desert dunes*. Dover Publication Inc. https://doi.org/10.1007/978-94-009-5682-7

Baker, A. R., & Jickells, T. D. (2006). Mineral particle size as a control on aerosol iron solubility. *Geophysical Research Letters*, *33*(17), 1–4. https://doi.org/10.1029/2006GL026557

Betzer, P. R., Carder, K. L., Duce, R. A., Merrill, J. T., Tindale, N. W., Uematsu, M., et al. (1988). Long–range transport of giant mineral aerosol particles. *Nature*, *336*(6199), 568–571. https://doi.org/10.1038/336568a0

Bhattachan, A., Okin, G. S., Zhang, J., Vimal, S., & Lettenmaier, D. P. (2019). Characterizing the role of wind and dust in traffic accidents in California. *GeoHealth*, *3*(10), 328–336. https://doi.org/10.1029/2019GH000212

Börker, J., Hartmann, J., Amann, T., & Romero-Mujalli, G. (2018). Terrestrial sediments of the earth: Development of a global unconsolidated sediments map database (gum). *Geochemistry, Geophysics, Geosystems*, *19*(4), 997–1024. https://doi.org/10.1002/2017GC007273

Brodrick, P., Okin, G., Ochoa, F., Thompson, D., Clark, R., Ehlmann, B., et al. (2025). EMIT L3 aggregated mineral spectral abundance and uncertainty 0.5 deg V002 [Dataset]. *NASA Land Processes Distributed Active Archive Center*. https://doi.org/10.5067/EMIT/EMITL3ASA.002

Brodrick, P. G., Clark, R. N., Swayze, G. A., Ehlman, B., Keebler, A., Thompson, D. R., & Green, R. O. (2023). *Earth surface mineral dust source InvesTigation (EMIT) EMIT L2b algorithm: Mineral detection and related products at the pixel Scale theoretical basis*. Pasadena.

Brodrick, P. G., Green, R. O., Thompson, D. R., Mahowald, N. M., Clark, R. N., Swayze, G. A., et al. (2023). *The Earth surface mineral dust source investigation (EMIT): Global distributions of mineralogy in arid lands* (pp. 11–15). American Geophysical Union Fall Meeting.

Brodrick, P. G., Okin, G., Ochoa, F., Thompson, D., Clark, R., Ehlmann, B., et al. (2023). EMIT L3 aggregated mineral spectral abundance and uncertainty 0.5 deg V001 [Dataset]. https://doi.org/10.5067/EMIT/EMITL3ASA.001

Brodsky, H., Calderón, R., Hamilton, D. S., Li, L., Miles, A., Pavlick, R., et al. (2023). Assessing long-distance atmospheric transport of soilborne plant pathogens. *Environmental Research Letters*, *18*(10), 104021. https://doi.org/10.1088/1748-9326/acf50c

Brown, R. J., Bonadonna, C., & Durant, A. J. (2012). A review of volcanic ash aggregation. *Physics and Chemistry of the Earth*, *45–46*, 65–78. https://doi.org/10.1016/j.pce.2011.11.001

Bullard, J. E. (2017). The distribution and biogeochemical importance of highlatitude dust in the Arctic and Southern Ocean- Antarctic regions. *Journal of Geophysical Research*, *122*(5), 3098–3103. https://doi.org/10.1002/2016JD026363

Chen, H., Laskin, A., Baltrusaitis, J., Gorski, C. A., Scherer, M. M., & Grassian, V. H. (2012). Coal fly ash as a source of iron in atmospheric dust. *Environmental Science & Technology*, *46*(4), 2112–2120. https://doi.org/10.1021/es204102f

Chiapello, I., Bergametti, B. M., Chatenet, B., Dulac, F., Jankowiak, I., Liousse, C., & Soares, E. S. (1999). Contribution of the different aerosol species to the aerosol mass load and optical depth over the northeastern tropical Atlantic. *Journal of Geophysical Research*, *104*(D4), 4025–4035. https://doi.org/10.1029/1998JD200044

Claquin, T., Schulz, M., & Balkanski, Y. (1999). Modeling the mineralogy of atmospheric dust sources. *Journal of Geophysical Research*, *104*(D18), 22243–22256. https://doi.org/10.1016/S1352-2310(03)00506-5

Clark, R. N. (2024). PSI-edu/spectroscopy-tetracorder: Tetracorder 5.27 with expert systems to 5.27e + specpr, spectral libraries, and radiative transfer models (v5.27.0). *Zenodo*. https://doi.org/10.5281/zenodo.11204505

Clark, R. N., & Roush, T. L. (1984). Reflectance spectroscopy: Quantitative analysis techniques for remote sensing applications. *Journal of Geophysical Research*, *89*(B7), 6329–6340. https://doi.org/10.1029/JB089iB07p06329

Clark, R. N., Swayze, G. A., Eric Livo, K., Brodrick, P. G., Dobrea, E. N., Vijayarangan, S., et al. (2024). Imaging spectroscopy: Earth and planetary remote sensing with the PSI tetracorder and expert systems from rovers to EMIT and beyond. *The Planetary Science Journal*, *5*(12), 276. https://doi.org/10.3847/PSJ/ad6c3a

Comola, F., Kok, J. F., Chamecki, M., & Martin, R. L. (2019). The intermittency of wind-driven sand transport. *Geophysical Research Letters*, *46*(22), 13430–13440. https://doi.org/10.1029/2019GL085739

Darmenova, K., Sokolik, I. N., Shao, Y., Marticorena, B., & Bergametti, G. (2009). Development of a physically based dust emission module within the weather research and forecasting (WRF) model: Assessment of dust emission parameterizations and input parameters for source regions in central and east Asia. *Journal of Geophysical Research*, *114*(14). https://doi.org/10.1029/2008JD011236

DeMott, P. J., Sassen, K., Poellot, M. R., Baumgardner, D., Rogers, D. C., Brooks, S. D., et al. (2003). African dust aerosols as atmospheric ice nuclei. *Geophysical Research Letters*, *30*(14), 1732. https://doi.org/10.1029/2003GL017410

Di Biagio, C., Balkanski, Y., Albani, S., Boucher, O., & Formenti, P. (2020). Direct radiative effect by mineral dust aerosols constrained by new microphysical and spectral optical data. *Geophysical Research Letters*, *47*(2), e2019GL086186. https://doi.org/10.1029/2019GL086186

Drakaki, E., Amiridis, V., Tsekeri, A., Gkikas, A., Proestakis, E., Drakaki, C. E., et al. (2022). Modeling coarse and giant desert dust particles. *Atmospheric Chemistry and Physics*, *22*(18), 12727–12748. https://doi.org/10.5194/acp-22-12727-2022

Dubovik, O., Smirnov, A., Holben, B. N., King, M. D., Kaufman, Y. J., Eck, T. F., & Slutsker, I. (2000). Accuracy assessments of aerosol optical properties retrieved from Aerososl Robotic Network (AERONET) Sun and sky radiance measurments. *Journal of Geophysical Research*, *105*(D8), 9791–9806. https://doi.org/10.1029/2000JD900040

Dupont, S., Bergametti, G., Marticorena, B., & Simoëns, S. (2013). Modeling saltation intermittency. *Journal of Geophysical Research: Atmospheres*, *118*(13), 7109–7128. https://doi.org/10.1002/jgrd.50528

Easter, R. C., Ghan, S. J., Zhang, Y., Saylor, R. D., Chapman, E. G., Laulainen, N. S., et al. (2004). MIRAGE: Model description and evaluation of aerosols and trace gases. *Journal of Geophysical Research D: Atmospheres*, *109*(20), 1–46. https://doi.org/10.1029/2004JD004571

Evan, A., Walkowiak, B., & Frouin, R. (2022). On the misclassification of dust as cloud at an AERONET site in the sonoran desert. *Journal of Atmospheric and Oceanic Technology*, *39*(2), 181–191. https://doi.org/10.1175/JTECH-D-21-0114.1

Eyring, V., Bony, S., Meehl, G. A., Senior, C. A., Stevens, B., Stouffer, R. J., & Taylor, K. E. (2016). Overview of the Coupled Model Intercomparison Project Phase 6 (CMIP6) experimental design and organization. *Geoscientific Model Development*, *9*(5), 1937–1958. https://doi.org/10.5194/gmd-9-1937-2016

Falkovich, A. H., Ganor, E., Levin, Z., Formenti, P., & Rudich, Y. (2001). Chemical and mineralogical analysis of individual mineral dust particles. *Journal of Geophysical Research*, *106*(D16), 18029–18036. https://doi.org/10.1029/2000JD900430

Fécan, F., Marticorena, B., & Bergametti, G. (1998). Parametrization of the increase of the aeolian erosion threshold wind friction velocity due to soil moisture for arid and semi-arid areas. *Annales Geophysicae*, *17*(1), 149–157. https://doi.org/10.1007/s00585-999-0149-7

Feng, Y., Wang, H., Rasch, P. J., Zhang, K., Lin, W., Tang, Q., et al. (2022). Global dust cycle and direct radiative effect in E3SM version 1: Impact of increasing model resolution. *Journal of Advances in Modeling Earth Systems*, *14*(7), e2021MS002909. https://doi.org/10.1029/2021MS002909

Formenti, P., Andreae, M. O., Lange, L., Roberts, G., Cafmeyer, J., Rajta, I., et al. (2001). Saharan dust in Brazil and Suriname during the large-scale Biosphere-Atmosphere Experiment in Amazonia (LBA)-Cooperative LBA Regional Experiment (CLAIRE) in March 1998. *Journal of Geophysical Research*, *106*(D14), 14919–14934. https://doi.org/10.1029/2000jd900827

Formenti, P., & Di Biagio, C. (2023a). Large synthesis of in situ field measurements of the size distribution of mineral dust aerosols across their lifecycle-LRT [Dataset]. *EaSy Data*. https://doi.org/10.57932/17dc781c-3e9d-4908-85b5-5c99e68e8f79

Formenti, P., & Di Biagio, C. (2023b). Large synthesis of in situ field measurements of the size distribution of mineral dust aerosols across their lifecycle-SOURCE [Dataset]. *EaSy Data*. https://doi.org/10.57932/58dbe908-9394-4504-9099-74a3e77140e9

Formenti, P., & Di Biagio, C. (2023c). Large synthesis of in situ field measurements of the size distribution of mineral dust aerosols across their lifecycle- MRT [Dataset]. *EaSy Data*. https://doi.org/10.57932/31f2adf7-74fb-48e8-a3ef-059f663c47f1

Formenti, P., & Di Biagio, C. (2024). Large synthesis of in situ field measurements of the size distribution of mineral dust aerosols across their life cycles. *Earth System Science Data*, *16*(11), 4995–5007. https://doi.org/10.5194/essd-16-4995-2024

Gelaro, R., McCarty, W., Suárez, M. J., Todling, R., Molod, A., Takacs, L., et al. (2017). The modern-era retrospective analysis for research and applications, version 2 (MERRA-2). *Journal of Climate*, *30*(14), 5419–5454. https://doi.org/10.1175/JCLI-D-16-0758.1

Ghan, S. J., & Zaveri, R. A. (2007). Parameterization of optical properties for hydrated internally mixed aerosol. *Journal of Geophysical Research*, *112*(10), 1–10. https://doi.org/10.1029/2006JD007927

Ginoux, P. (2003). Effects of nonsphericity on mineral dust modeling. *Journal of Geophysical Research*, *108*(D2), 4052. https://doi.org/10.1029/2002jd002516

Ginoux, P., Chin, M., Tegen, I., Prospero, J. M., Holben, B. N., Dubovik, O., & Lin, S.-J. (2001). Sources and distribution of dust aerosols with the GOCART model. *Journal of Geophysical Research*, *106*(D17), 20255–20273. https://doi.org/10.1029/2000JD000053

Gliß, J., Mortier, A., Schulz, M., Andrews, E., Balkanski, Y., Bauer, S. E., et al. (2021). AeroCom phase III multi-model evaluation of the aerosol life cycle and optical properties using ground- and space-based remote sensing as well as surface in situ observations. *Atmospheric Chemistry and Physics*, *21*(1), 87–128. https://doi.org/10.5194/acp-21-87-2021

Gonçalves Ageitos, M., Obiso, V., Miller, R. L., Jorba, O., Klose, M., Dawson, M., et al. (2023). Modeling dust mineralogical composition: Sensitivity to soil mineralogy atlases and their expected climate impacts. *Atmospheric Chemistry and Physics*, *23*(15), 8623–8657. https://doi.org/10.5194/acp-23-8623-2023

Goudie, A. S. (2014). Desert dust and human health disorders. *Environment International*, *63*, 101–113. https://doi.org/10.1016/j.envint.2013.10.011

Green, R. O., Mahowald, N., Ung, C., Thompson, D. R., Bator, L., Bennet, M., et al. (2020). The Earth surface mineral dust source investigation: An Earth science imaging spectroscopy Mission. *IEEE Aerospace Conference Proceedings*, 1–15. https://doi.org/10.1109/AERO47225.2020.9172731

Groot Zwaaftink, C. D., Grythe, H., Skov, H., & Stohl, A. (2016). Substantial contribution of northern high-latitude sources to mineral dust in the Arctic. *Journal of Geophysical Research*, *121*(22), 13678–13697. https://doi.org/10.1002/2016JD025482

Hapke, B. (1981). Bidirectional reflectance spectroscopy: 1. Theory. *Journal of Geophysical Research*, *86*(B4), 3039–3054. https://doi.org/10.1029/jb086ib04p03039

Heisel, M., Chen, B., Kok, J. F., & Chamecki, M. (2021). Gentle topography increases vertical transport of coarse dust by orders of magnitude. *Journal of Geophysical Research: Atmospheres*, *126*(14), 1–16. https://doi.org/10.1029/2021jd034564

Huang, Y., Kok, J. F., Kandler, K., Lindqvist, H., Nousiainen, T., Sakai, T., et al. (2020). Climate models and remote sensing retrievals neglect substantial desert dust asphericity. *Geophysical Research Letters*, *47*(6), 1–11. https://doi.org/10.1029/2019GL086592

Huang, Y., Kok, J. F., Saito, M., & Muñoz, O. (2023). Single-scattering properties of ellipsoidal dust aerosols constrained by measured dust shape distributions. *Atmospheric Chemistry and Physics*, *23*(4), 2557–2577. https://doi.org/10.5194/acp-23-2557-2023

Huneeus, N., Schulz, M., Balkanski, Y., Griesfeller, J., Prospero, J., Kinne, S., et al. (2011). Global dust model intercomparison in AeroCom phase i. *Atmospheric Chemistry and Physics*, *11*(15), 7781–7816. https://doi.org/10.5194/acp-11-7781-2011

Jickells, T. D., An, Z. S., Andersen, K. K., Baker, A. R., Bergametti, C., Brooks, N., et al. (2005). Global iron connections between desert dust, ocean biogeochemistry, and climate. *Science*, *308*(5718), 67–71. https://doi.org/10.1126/science.1105959

Jones, A. C., Hill, A., Hemmings, J., Lemaitre, P., Quérel, A., Ryder, C. L., & Woodward, S. (2022). Below-cloud scavenging of aerosol by rain: A review of numerical modelling approaches and sensitivity simulations with mineral dust in the Met Office's Unified Model. *Atmospheric Chemistry and Physics*, *22*(17), 11381–11407. https://doi.org/10.5194/acp-22-11381-2022

Journet, E., Balkanski, Y., & Harrison, S. (2014). A new data set of soil mineralogy for dust-cycle modeling. *Atmospheric Chemistry and Physics*, *14*(8), 2014–3801. https://doi.org/10.5194/acp-14-3801-2014

Kalashnikova, O. V., & Sokolik, I. N. (2004). Modeling the radiative properties of nonspherical soil-derived mineral aerosols. *Journal of Quantitative Spectroscopy and Radiative Transfer*, *87*(2), 137–166. https://doi.org/10.1016/j.jqsrt.2003.12.026

Kandler, K., Benker, N., Bundke, U., Cuevas, E., Ebert, M., Knippertz, P., et al. (2007). Chemical composition and complex refractive index of Saharan Mineral Dust at Izaña, Tenerife (Spain) derived by electron microscopy. *Atmospheric Environment*, *41*(37), 8058–8074. https://doi.org/10.1016/j.atmosenv.2007.06.047

Kandler, K., Schütz, L., Deutscher, C., Ebert, M., Hofmann, H., Jäckel, S., et al. (2009). Size distribution, mass concentration, chemical and mineralogical composition and derived optical parameters of the boundary layer aerosol at Tinfou, Morocco, during SAMUM 2006. *Tellus Series B Chemical and Physical Meteorology*, *61*(1), 32–50. https://doi.org/10.1111/j.1600-0889.2008.00385.x

Karyampudi, V. M., Palm, S. P., Reagen, J. A., Fang, H., Grant, W. B., Hoff, R. M., et al. (1999). Validation of the Saharan dust plume conceptual model using lidar, Meteosat, and ECMWF data. *Bulletin of the American Meteorological Society*, *80*(6), 1045–1075. https://doi.org/10.1175/1520-0477(1999)080<1045:VOTSDP>2.0.CO;2

Karydis, V. A., Kumar, P., Barahona, D., Sokolik, I. N., & Nenes, A. (2011). On the effect of dust particles on global cloud condensation nuclei and cloud droplet number. *Journal of Geophysical Research*, *116*(23), D23204.1. https://doi.org/10.1029/2011JD016283

Ke, Z., Liu, X., Wu, M., Shan, Y., & Shi, Y. (2022). Improved dust representation and impacts on dust transport and radiative effect in CAM5. https://doi.org/10.1029/2021MS002845

Kellogg, C. A., & Griffin, D. W. (2006). Aerobiology and the global transport of desert dust. *Trends in Ecology & Evolution*, *21*(11), 638–644. https://doi.org/10.1016/j.tree.2006.07.004

Klose, M., Jorba, O., Ageitos, M. G., Escribano, J., Dawson, M. L., Obiso, V., et al. (2021). Mineral dust cycle in the Multiscale Online Non-hydrostatic AtmospheRe CHemistry model (MONARCH) Version 2. 0. *Geoscientific Model Development*, *14*(10), 6403–6444. https://doi.org/10.5194/gmd-14-6403-2021

Kok, J. F. (2011a). A scaling theory for the size distribution of emitted dust aerosols suggests climate models underestimate the size of the global dust cycle. *Proceedings of the National Academy of Science USA*, *108*(3), 1016–1021. https://doi.org/10.1073/pnas.1014798108

Kok, J. F. (2011b). Does the size distribution of mineral dust aerosols depend on the wind speed at emission? *Atmospheric Chemistry and Physics*, *11*(19), 10149–10156. https://doi.org/10.5194/acp-11-10149-2011

Kok, J. F., Adebiyi, A. A., Albani, S., Balkanski, Y., Checa-Garcia, R., Chin, M., et al. (2021a). Contribution of the world's main dust source regions to the global cycle of desert dust. *Atmospheric Chemistry and Physics*, *21*(10), 8169–8193. https://doi.org/10.5194/acp-21-8169-2021

Kok, J. F., Adebiyi, A. A., Albani, S., Balkanski, Y., Checa-Garcia, R., Chin, M., et al. (2021b). Improved representation of the global dust cycle using observational constraints on dust properties and abundance. *Atmospheric Chemistry and Physics*, *21*(10), 8127–8167. https://doi.org/10.5194/acp-21-8127-2021

Kok, J. F., Albani, S., Mahowald, N. M., & Ward, D. S. (2014). An improved dust emission model—Part 2: Evaluation in the Community Earth System Model, with implications for the use of dust source functions. *Atmospheric Chemistry and Physics*, *14*(23), 13043–13061. https://doi.org/10.5194/acp-14-13043-2014

Kok, J. F., Mahowald, N. M., Fratini, G., Gillies, J. A., Ishizuka, M., Leys, J. F., et al. (2014). An improved dust emission model—Part 1: Model description and comparison against measurements. *Atmospheric Chemistry and Physics*, *14*(23), 13023–13041. https://doi.org/10.5194/acp-14-13023-2014

Kok, J. F., Parteli, E., Michaels, T., & Karam, D. (2012). The physics of wind blown sand and dust. *Reports on Progress in Physics*, *75*(10), 106901. https://doi.org/10.1088/0034-4885/75/10/106901

Kok, J. F., Ridley, D. A., Zhou, Q., Miller, R. L., Zhao, C., Heald, C. L., et al. (2017). Smaller desert dust cooling effect estimated from analysis of dust size and abundance. *Nature Geoscience*, *10*(4), 274–278. https://doi.org/10.1038/ngeo2912

Kok, J. F., Storelvmo, T., Karydis, V. A., Adebiyi, A. A., Mahowald, N. M., Evan, A. T., et al. (2023). Mineral dust aerosol impacts on global climate and climate change. *Nature Reviews Earth & Environment*, *4*(2), 71–86. https://doi.org/10.1038/s43017-022-00379-5

Langmann, B. (2013). Volcanic ash versus mineral dust: Atmospheric processing and environmental and climate impacts. *ISRN Atmospheric Sciences*, *2013*, 1–17. https://doi.org/10.1155/2013/245076

Lawrence, C. R., & Neff, J. (2009). The contemporary physical and chemical flux of Aeolian dust: A synthesis of direct measurements of dust deposition. *Chemical Geology*, *257*(1–2), 46–63. https://doi.org/10.1016/j.chemgeo.2009.02.005

Leung, D. M., Kok, J. F., Li, L., Mahowald, N. M., Lawrence, D. M., Tilmes, S., et al. (2024). A new process-based and scale-aware desert dust emission scheme for global climate models – Part II: Evaluation in the Community Earth System Model version 2 (CESM2). *Atmospheric Chemistry and Physics*, *24*(4), 2287–2318. https://doi.org/10.5194/acp-24-2287-2024

Leung, D. M., Kok, J. F., Li, L., Okin, G. S., Prigent, C., Klose, M., et al. (2023). A new process-based and scale-aware desert dust emission scheme for global climate models – Part I: Description and evaluation against inverse modeling emissions. *Atmospheric Chemistry and Physics*, *23*(4), 6487–6523. https://doi.org/10.5194/acp-23-6487-2023

Levy, R. C., Remer, L. A., Kleidman, R. G., Mattoo, S., Ichoku, C., Kahn, R., & Eck, T. F. (2010). Global evaluation of the Collection 5 MODIS dark-target aerosol products over land. *Atmospheric Chemistry and Physics*, *10*(21), 10399–10420. https://doi.org/10.5194/acp-10-10399-2010

Li, L. (2025). MAM10 code for "Modeling Large Dust Aerosols in the Community Earth System Model Version 2 (CESM2)" [Software]. *Zenodo*. https://doi.org/10.5281/zenodo.16878107

Li, L. (2026). Dust-Related quantities simulated by MAM10 for modeling large dust aerosols in the community Earth System model version 2 (CESM2) [Dataset]. *Zenodo*. https://doi.org/10.5281/zenodo.18176766

Li, L., Mahowald, N. M., Gonçalves Ageitos, M., Obiso, V., Miller, R. L., Pérez García-Pando, C., et al. (2024). Improved constraints on hematite refractive index for estimating climatic effects of dust aerosols. *Communications Earth & Environment*, *5*(1), 295. https://doi.org/10.1038/s43247-024-01441-4

Li, L., Mahowald, N. M., Kok, J. F., Liu, X., Wu, M., Leung, D. M., et al. (2022a). Data and codes for "Importance of different parameterization changes for the updated dust cycle modelling in the Community Atmosphere Model (version 6.1)" [Software]. *Zenodo*. https://doi.org/10.5281/zenodo.6989502

Li, L., Mahowald, N. M., Kok, J. F., Liu, X., Wu, M., Leung, D. M., et al. (2022b). Importance of different parameterization changes for the updated dust cycle modeling in the Community Atmosphere Model (version 6.1). *Geoscientific Model Development*, *15*(22), 8181–8219. https://doi.org/10.5194/gmd-15-8181-2022

Li, L., Mahowald, N. M., Miller, R. L., Pérez García-Pando, C., Gonçalves Ageitos, M., Ginoux, P., et al. (2025). Spaceborne mineral mapping reduces dust's shortwave radiative impact uncertainty. *EarthArXiv*, 2–28. https://doi.org/10.31223/X57Q97

Li, L., Mahowald, N. M., Miller, R. L., Pérez García-Pando, C., Klose, M., Hamilton, D. S., et al. (2021). Quantifying the range of the dust direct radiative effect due to source mineralogy uncertainty. *Atmospheric Chemistry and Physics*, *21*(5), 3973–4005. https://doi.org/10.5194/acp-21-3973-2021

Li, L., Mahowald, N. M., Obiso, V., Kok, J. F., Miller, R. L., Liu, X., et al. (2025). Dust direct radiative effect including large particles and component minerals. *Geophysical Research Letters*, *52*(22), e2025GL119383. https://doi.org/10.1029/2025GL119383

Li, L., & Sokolik, I. N. (2018). Analysis of dust aerosol retrievals using satellite data in Central Asia. *Atmosphere*, *9*(8), 288. https://doi.org/10.3390/atmos9080288

Liao, H., & Seinfeld, J. H. (1998). Radiative forcing by mineral dust aerosols: Sensitivity to key variables. *Journal of Geophysical Research*, *103*(D24), 631–637. https://doi.org/10.1029/1998jd200036

Liu, D., Ishizuka, M., Mikami, M., & Shao, Y. (2018). Turbulent characteristics of saltation and uncertainty of saltation model parameters. *Atmospheric Chemistry and Physics*, *18*(10), 7595–7606. https://doi.org/10.5194/acp-18-7595-2018

Liu, X., Easter, R. C., Ghan, S. J., Zaveri, R., Rasch, P., Shi, X., et al. (2012). Toward a minimal representation of aerosols in climate models: Description and evaluation in the Community Atmosphere Model CAM5. *Geoscientific Model Development*, *5*(3), 709–739. https://doi.org/10.5194/gmd-5-709-2012

Liu, X., Ma, P. L., Wang, H., Tilmes, S., Singh, B., Easter, R. C., et al. (2016). Description and evaluation of a new four-mode version of the Modal Aerosol Module (MAM4) within version 5.3 of the Community Atmosphere Model. *Geoscientific Model Development*, *9*(2), 505–522. https://doi.org/10.5194/gmd-9-505-2016

Longo, A. F., Feng, Y., Lai, B., Landing, W. M., Shelley, R. U., Nenes, A., et al. (2016). Influence of atmospheric processes on the solubility and composition of iron in Saharan dust. *Environmental Science and Technology*, *50*(13), 6912–6920. https://doi.org/10.1021/acs.est.6b02605

Lu, L., Li, L., Rathod, S., Hess, P., Martínez, C., Fernandez, N., et al. (2024). Characterizing the atmospheric Mn cycle and its impact on terrestrial biogeochemistry. *Global Biogeochemical Cycles*, *38*(4), e2023GB007967. https://doi.org/10.1029/2023GB007967

Luo, C., Mahowald, N., Bond, T., Chuang, P. Y., Artaxo, P., Siefert, R., et al. (2008). Combustion iron distribution and deposition. *Global Biogeochemical Cycles*, *22*(1), GB1012. https://doi.org/10.1029/2007GB002964

Mahowald, N. M. (2011). Aerosol indirect effect on biogeochemical cycles and climate. *Science*, *334*(November), 1500–1796. https://doi.org/10.1126/science.1207374

Mahowald, N. M., Albani, S., Kok, J. F., Engelstaeder, S., Scanza, R., Ward, D. S., & Flanner, M. G. (2014). The size distribution of desert dust aerosols and its impact on the Earth system. *Aeolian Research*, *15*, 53–71. https://doi.org/10.1016/j.aeolia.2013.09.002

Mahowald, N. M., Baker, A. R., Bergametti, G., Brooks, N., Duce, R. A. R. A., Jickells, T. D. T. D., et al. (2005). Atmospheric global dust cycle and iron inputs to the ocean. *Global Biogeochemical Cycles*, *19*(4), GB4025. https://doi.org/10.1029/2004GB002402

Mahowald, N. M., Engelstaedter, S., Luo, C., Sealy, A., Artaxo, P., Benitez-Nelson, C., et al. (2009). Atmospheric Iron deposition: Global distribution, variability, and human perturbations. *Annual Review of Marine Science*, *1*(1), 245–278. https://doi.org/10.1146/annurev.marine.010908.163727

Mahowald, N. M., Hamilton, D. S., Mackey, K. R. M., Moore, J. K., Baker, A. R., Scanza, R. A., & Zhang, Y. (2018). Aerosol trace metal leaching and impacts on marine microorganisms. *Nature Communications*, *9*(1), 2614. https://doi.org/10.1038/s41467-018-04970-7

Mahowald, N. M., Kloster, S., Engelstaedter, S., Moore, J. K., Mukhopadhyay, S., McConnell, J. R., et al. (2010). Observed 20th century desert dust variability: Impact on climate and biogeochemistry. *Atmospheric Chemistry and Physics*, *10*(22), 10875–10893. https://doi.org/10.5194/acp-10-10875-2010

Mahowald, N. M., Li, L., Albani, S., Hamilton, D. S., & Kok, J. F. (2024). Opinion: The importance of historical and paleoclimate aerosol radiative effects. *Atmospheric Chemistry and Physics*, *24*(1), 533–551. https://doi.org/10.5194/acp-24-533-2024

Mahowald, N. M., Li, L., Vira, J., Prank, M., Hamilton, D. S., Matsui, H., et al. (2024). Datasets for: AERO-MAP: A data compilation and modelling approach to understand the fine and coarse mode aerosol composition [Dataset]. *Zenodo*. https://doi.org/10.5281/zenodo.15391280

Mahowald, N. M., Li, L., Vira, J., Prank, M., Hamilton, D. S., Matsui, H., et al. (2025). AERO-MAP: A data compilation and modeling approach to understand spatial variability in fine- and coarse-mode aerosol composition. *Atmospheric Chemistry and Physics*, *25*(9), 4665–4702. https://doi.org/10.5194/acp-25-4665-2025

Mahowald, N. M., Muhs, D., Levis, S., Rasch, P. J., Yoshioka, M., Zender, C. S., & Luo, C. (2006). Change in atmospheric mineral aerosols in response to climate: Last glacial period, pre-industrial, modern and doubled-carbon dioxide climates. *Journal of Geophysical Research*, *111*(10), D10202. https://doi.org/10.1029/2005JD006653

Maki, T., Noda, J., Morimoto, K., Aoki, K., Kurosaki, Y., Huang, Z., et al. (2022). Long-range transport of airborne bacteria over East Asia: Asian dust events carry potentially nontuberculous Mycobacterium populations. *Environment International*, *168*, 107471. https://doi.org/10.1016/j.envint.2022.107471

Mallios, S. A., Drakaki, E., & Amiridis, V. (2020). Effects of dust particle sphericity and orientation on their gravitational settling in the earth's atmosphere. *Journal of Aerosol Science*, *150*(April), 1–21. https://doi.org/10.1016/j.jaerosci.2020.105634

Marticorena, B., & Bergametti, G. (1995). Modeling the atmospheric dust cycle: 1. Design of a soil-derived dust emission scheme. *Journal of Geophysical Research*, *100*(D8), 16415–16430. https://doi.org/10.1029/95JD00690

Mccutcheon, J., Lutz, S., Williamson, C., Joseph, M., Tedstone, A. J., Vanderstraeten, A., et al. (2021). Mineral phosphorus drives glacier algal blooms on the Greenland Ice Sheet. *Nature Communications*, *12*, 1–11. https://doi.org/10.1038/s41467-020-20627-w

Measures, C. I., & Vink, S. (2000). On the use of dissolved aluminum in surface waters to estimate dust deposition to the ocean. *Global Biogeochemical Cycles*, *14*(1), 317–327. https://doi.org/10.1029/1999GB001188

Meinander, O., Dagsson-Waldhauserova, P., Amosov, P., Aseyeva, E., Atkins, C., Baklanov, A., et al. (2022). Newly identified climatically and environmentally significant high-latitude dust sources. *Atmospheric Chemistry and Physics*, *22*(17), 11889–11930. https://doi.org/10.5194/acp-22-11889-2022

Meng, J., Huang, Y., Leung, D. M., Li, L., Adebiyi, A. A., Ryder, C. L., et al. (2022). Improved parameterization for the size distribution of emitted dust aerosols reduces model underestimation of super coarse dust. *Geophysical Research Letters*, *49*(8), 1–12. https://doi.org/10.1029/2021GL097287

Meskhidze, N., Chameides, W. L., & Nenes, A. (2005). Dust and pollution: A recipe for enhanced ocean fertilization? *Journal of Geophysical Research D: Atmospheres*, *110*(3), 1–23. https://doi.org/10.1029/2004JD005082

Meyer, H., Kandler, K., Dupont, S., Escribano, J., Girdwood, J., Nikolich, G., et al. (2026). From fine to giant: Multi-instrument assessment of the dust particle size distribution at an emission source during the J-WADI field campaign. *Atmospheric Measurement Techniques*, *19*(1), 21–61. https://doi.org/10.5194/amt-19-21-2026

Neale, R. B., Chen, C., Lauritzen, P. H., Williamson, D. L., Conley, A. J., Smith, A. K., et al. (2010). Description of the NCAR Community Atmosphere Model (CAM 5.0). In *NCAR technical note, Boulder, CO*.

Niimura, N., Okada, K., Fan, X.-B., Kai, K., Arao, K., Shi, G.-Y., & Takahashi, S. (1998). Formation of Asian dust-storm particles mixed internally with sea salt in the atmosphere. *Ournal of the Meteorological Society of Japan*, *76*(2), 275–288. https://doi.org/10.2151/jmsj1965.76.2_275

Obiso, V., Gonçalves Ageitos, M., Pérez García-Pando, C., Perlwitz, J. P., Schuster, G. L., Bauer, S. E., et al. (2024). Observationally constrained regional variations of shortwave absorption by iron oxides emphasize the cooling effect of dust. *Atmospheric Chemistry and Physics*, *24*(9), 5337–5367. https://doi.org/10.5194/acp-24-5337-2024

Okada, K., Naruse, H., Tanaka, T., Nemoto, O., Iwasaka, Y., Wu, P.-M., et al. (1990). X-ray spectrometry of individual Asian dust-storm particles over the Japanese islands and the North Pacific Ocean. *Atmospheric Environment, Part A: General Topics*, *24*(6), 1369–1378. https://doi.org/10.1016/0960-1686(90)90043-M

Okin, G. S. (2008). A new model of wind erosion in the presence of vegetation. *Journal of Geophysical Research*, *113*(F02S10), 1–11. https://doi.org/10.1029/2007JF000758

Okin, G. S., Ochoa, F., Brodrick, P. G., Thompson, D. R., Keebler, A., Ehlmann, B. L., et al. (2023). EMIT L3 algorithm: Aggregated mineral spectral abundance theoretical basis, Pasadena, California.

Osada, K. (2013). Water soluble fraction of Asian dust particles Laser Intensity before Height μm after. *Atmospheric Research*, *124*, 101–108. https://doi.org/10.1016/j.atmosres.2013.01.001

Panta, A., Kandler, K., Alastuey, A., González-Flórez, C., González-Romero, A., Klose, M., et al. (2023). Insights into the single particle composition, size, mixing state and aspect ratio of freshly emitted mineral dust from field measurements in the Moroccan Sahara using electron microscopy. *Atmospheric Chemistry and Physics*, *23*(6), 3861–3885. https://doi.org/10.5194/acp-23-3861-2023

Pérez García-Pando, C., Stanton, M. C., Diggle, P. J., Trzaska, S., Miller, R. L., Perlwitz, J. P., et al. (2014). Soil dust aerosols and wind as predictors of seasonal Meningitis incidence. *Environmental Health Perspectives*, *122*(7), 679–686. https://doi.org/10.1289/ehp.1306640

Perlwitz, J. P., Pérez García-Pando, C., & Miller, R. L. (2015a). Predicting the mineral composition of dust aerosols—Part 1: Representing key processes. *Atmospheric Chemistry and Physics*, *15*(20), 11593–11627. https://doi.org/10.5194/acp-15-11593-2015

Perlwitz, J. P., Pérez García-Pando, C., & Miller, R. L. (2015b). Predicting the mineral composition of dust aerosols—Part 2: Model evaluation and identification of key processes with observations. *Atmospheric Chemistry and Physics*, *15*(20), 11629–11652. https://doi.org/10.5194/acp-15-11629-2015

Petroff, A., & Zhang, L. (2010). Development and validation of a size-resolved particle dry deposition scheme for application in aerosol transport models. *Geoscientific Model Development*, *3*(2), 753–769. https://doi.org/10.5194/gmd-3-753-2010

Pierre, C., Bergametti, G., Marticorena, B., Kergoat, L., Mougin, E., & Hiernaux, P. (2014). Comparing drag partition schemes over a herbaceous Sahelian rangeland. *Journal of Geophysical Research: Earth Surface*, *119*(10), 2291–2313. https://doi.org/10.1002/2014JF003177

Prigent, C., Tegen, I., Aires, F., Marticorena, B., & Zribi, M. (2005). Estimation of the aerodynamic roughness length in arid and semi-arid regions over the globe with the ERS scatterometer. *Journal of Geophysical Research D: Atmospheres*, *110*(9), 1–12. https://doi.org/10.1029/2004JD005370

Prospero, J. M., Bonatti, E., Schubert, C., & Carlson, T. N. (1970). Dust in the Caribbean atmosphere traced to an African dust storm. *Earth and Planetary Science Letters*, *9*(3), 287–293. https://doi.org/10.1016/0012-821X(70)90039-7

Prospero, J. M., Olmez, I., & Ames, M. (2001). Al and Fe in PM 2.5 and PM 10 suspended particles in south-central Florida: The impact of the long range transport of African mineral dust. *Water, Air, & Soil Pollution*, *125*(1), 291–317. https://doi.org/10.1023/A:1005277214288

Ratcliffe, N. G., Ryder, C. L., Bellouin, N., Woodward, S., Jones, A., Johnson, B., et al. (2024). Long-range transport of coarse mineral dust: An evaluation of the Met Office Unified Model against aircraft observations. *Atmospheric Chemistry and Physics*, *24*(21), 12161–12181. https://doi.org/10.5194/acp-24-12161-2024

Reid, E., Reid, J., Meier, M., Dunlap, M., Cliff, S., Broumas, A., et al. (2003). Characterization of African dust transported to Puerto Rico by individual particle and size segregated bulk analysis. *Journal of Geophysical Research*, *108*(D198591), 1–22. https://doi.org/10.1029/2002jd002935

Reid, J. S., Jonsson, H. H., Maring, H. B., Smirnov, A., Savoie, D. L., Cliff, S. S., et al. (2003). Comparison of size and morphological measurements of coarse mode dust particles from Africa. *Journal of Geophysical Research D: Atmospheres*, *108*(D19), 8593. https://doi.org/10.1029/2002jd002485

Reid, J. S., Westphal, D. L., Livingston, J. M., Savoie, D. L., Maring, H. B., Jonsson, H. H., et al. (2002). Dust vertical distribution in the Caribbean during the Puerto Rico dust experiment. *Geophysical Research Leters*, *29*(7), 1–4. https://doi.org/10.1029/2001GL014092

Ridley, A. D., Heald, L. C., Kok, F. J., & Zhao, C. (2016). An observationally constrained estimate of global dust aerosol optical depth. *Atmospheric Chemistry and Physics*, *16*(23), 15097–15117. https://doi.org/10.5194/acp-16-15097-2016

Rodakoviski, R., Kok, J., & Chamecki, M. (2023). Dust settling from turbulent layers in the free troposphere: Implications for the Saharan air layer. *Journal of Geophysical Research: Atmospheres*, *128*(6), e2022JD037724. https://doi.org/10.1029/2022JD037724

Rosenberg, P., Parker, D., Ryder, C., Marsham, J., Garcia-Carreras, L., Dorsey, J., et al. (2014). Quantifying particle size and turbulent scale dependence of dust flux in the Sahara using air craft measurements. *Journal of Geophysical Research*, *119*(12), 7577–7598. https://doi.org/10.1002/2013JD021255

Ryder, C. L., Highwood, E. J., Rosenberg, P. D., Trembath, J., Brooke, J. K., Bart, M., et al. (2013). Optical properties of Saharan dust aerosol and contribution from the coarse mode as measured during the Fennec 2011 aircraft campaign. *Atmospheric Chemistry and Physics*, *13*(1), 303–325. https://doi.org/10.5194/acp-13-303-2013

Ryder, C. L., Highwood, E. J., Walser, A., Seibert, P., Philipp, A., & Weinzierl, B. (2019). Coarse and giant particles are ubiquitous in Saharan dust export regions and are radiatively significant over the Sahara. *Atmospheric Chemistry and Physics*, *19*(24), 15353–15376. https://doi.org/10.5194/acp-19-15353-2019

Ryder, C. L., Marenco, F., Brooke, J. K., Estelles, V., Cotton, R., Formenti, P., et al. (2018). Coarse-mode mineral dust size distributions, composition and optical properties from AER-D aircraft measurements over the tropical eastern Atlantic. *Atmospheric Chemistry and Physics*, *18*(23), 17225–17257. https://doi.org/10.5194/acp-18-17225-2018

Scanza, R. A., Mahowald, N., Ghan, S., Zender, C. S., Kok, J. F., Liu, X., et al. (2015). Modeling dust as component minerals in the Community Atmosphere Model: Development of framework and impact on radiative forcing. *Atmospheric Chemistry and Physics*, *15*(1), 537–561. https://doi.org/10.5194/acp-15-537-2015

Shao, Y. (2008). *Physics and modelling of wind erosion. Physics and modelling of wind erosion* (2nd ed.). Springer. https://doi.org/10.1007/978-1-4020-8895-7

Shi, Y., Liu, X., Wu, M., Ke, Z., & Brown, H. (2021). Relative importance of high-latitude local and long-range transported dust to Arctic ice nucleating particles and impacts on Arctic mixed-phase clouds. In *Atmospheric Chemistry and Physics Discussions* (pp. 1–57). https://doi.org/10.5194/acp-2021-621

Shinn, E., Smith, G., Prospero, J., Betzer, P., Hayes, M., Garrison, V., & Barber, R. (2000). African dust and the demise of the Carbbean Coral Reefs. *Geophysical Research Letterrs*, *27*(19), 3029–3032. https://doi.org/10.1029/2000gl011599

Sokolik, I. N., & Toon, O. B. (1999). Incorporation of mineralogical composition into models of the radiative properties of mineral aerosol from UV to IR wavelengths. *Journal of Geophysical Research*, *104*(D8), 9423–9444. https://doi.org/10.1029/1998JD200048

Stokes, G. G. (1851). On the effect of the internal friction of fluids on the motion of a pendulum. *Transactions of the Cambridge Philosophical Society*, *8*, 9.

Tegen, I., Harrison, S. P., Kohfeld, K., Prentice, C., Coe, M., & Heimann, M. (2002). The impact of vegetation and preferential source areas on global dust aerosol: Results from a model study. *Journal of Geophysical Research*, *107*(D21), 4576–4597. https://doi.org/10.1029/2001JD000963

Thompson, D. R., Green, R. O., Bradley, C., Brodrick, P. G., Mahowald, N., Dor, E. B., et al. (2024). On-orbit calibration and performance of the EMIT imaging spectrometer. *Remote Sensing of Environment*, *303*, 113986. https://doi.org/10.1016/j.rse.2023.113986

Toth, J. R., Rajupet, S., Squire, H., Volbers, B., Zhou, J., Xie, L., et al. (2020). Electrostatic forces alter particle size distributions in atmospheric dust. *Atmospheric Chemistry and Physics*, *20*(5), 3181–3190. https://doi.org/10.5194/acp-20-3181-2020

Usher, C. R., Michel, A. E., & Grassian, V. H. (2003). Reactions on mineral dust. *Chemical Reviews*, *103*(12), 4883–4939. https://doi.org/10.1021/cr020657y

van der Does, M., Knippertz, P., Zschenderlein, P., Giles Harrison, R., & Stuut, J. B. W. (2018). The mysterious long-range transport of giant mineral dust particles. *Science Advances*, *4*(12), 1–9. https://doi.org/10.1126/sciadv.aau2768

van der Does, M., Korte, L. F., Munday, C. I., Brummer, G. J. A., & Stuut, J. B. W. (2016). Particle size traces modern Saharan dust transport and deposition across the equatorial North Atlantic. *Atmospheric Chemistry and Physics*, *16*(21), 13697–13710. https://doi.org/10.5194/acp-16-13697-2016

Wan, H., Zhang, K., Vogl, C. J., Woodward, C. S., Easter, R. C., Rasch, P. J., et al. (2024). Numerical coupling of aerosol emissions, dry removal, and turbulent mixing in the E3SM Atmosphere Model version 1 (EAMv1)—Part 1: Dust budget analyses and the impacts of a revised coupling scheme. *Geoscientific Model Development*, *17*(3), 1387–1407. https://doi.org/10.5194/gmd-17-1387-2024

Wang, H., Liu, X., Wu, C., Lin, G., Dai, T., Goto, D., et al. (2024). Larger dust cooling effect estimated from regionally dependent refractive indices. *Geophysical Research Letters*, *51*(9), e2023GL107647. https://doi.org/10.1029/2023GL107647

Warren, S. G., Roesler, C. S., Brandt, R. E., & Curran, M. (2019). Green icebergs revisited journal of geophysical research: Oceans. *Journal of Geophysical Research: Oceans*, *124*(2), 925–938. https://doi.org/10.1029/2018JC014479

Weinzierl, B., Ansmann, A., Prospero, J. M., Althausen, D., Benker, N., Chouza, F., et al. (2017). The Saharan aerosol long-range transport and aerosol-cloud-interaction ex-periment: Overview and selected highlights. *Bulletin of the American Meteorological Society*, *98*(7), 1427–1452. https://doi.org/10.1175/BAMS-D-15-00142.1

Weinzierl, B., Petzold, A., Esselborn, M., Wirth, M., Rasp, K., Kandler, K., et al. (2009). Airborne measurements of dust layer properties, particle size distribution and mixing state of Saharan dust during SAMUM 2006. *Tellus Series B Chemical and Physical Meteorology*, *61*(1), 96–117. https://doi.org/10.1111/j.1600-0889.2008.00392.x

Wong, M. Y., Rathod, S. D., Marino, R., Li, L., Howarth, R. W., Alastuey, A., et al. (2021). Anthropogenic perturbations to the Atmospheric molybdenum cycle. *Global Biogeochemical Cycles*, *35*(2), e2020GB006787. https://doi.org/10.1029/2020GB006787

Wu, M., Liu, X., Zhang, L., Wu, C., Lu, Z., Ma, P. L., et al. (2018). Impacts of aerosol dry deposition on Black carbon spatial distributions and radiative effects in the Community Atmosphere Model CAM5. *Journal of Advances in Modeling Earth Systems*, *10*(5), 1150–1171. https://doi.org/10.1029/2017MS001219

Zender, C., Bian, H., & Newman, D. (2003). Mineral Dust Entrainment and Deposition (DEAD) model: Description and 1990s dust climatology. *Journal of Geophysical Research*, *108*(D14), 4416. https://doi.org/10.1029/2002JD002775

Zender, C., Newman, D., & Torres, O. (2003). Spatial heterogeneity in aerolian erodibility: Uniform, topographic, geomorphic and hydrologic hypotheses. *Journal of Geophysical Research*, *108*(D17), 4543. https://doi.org/10.1029/2002JD003039

Zhang, D., Iwasaka, Y., & Shi, G. (2005). Sea salt shifts the range sizes of Asian dust. *Eos, Transactions American Geophysical Union*, *86*(50), 523. https://doi.org/10.1029/2005EO500003

Zhang, D., Iwasaka, Y., Shi, G., Zang, J., Matsuki, A., & Trochkine, D. (2003). Mixture state and size of Asian dust particles collected at southwestern Japan in spring 2000. *Journal of Geophysical Research*, *108*, D24. https://doi.org/10.1029/2003JD003869

Zhang, L., Gong, S., Padro, J., & Barrie, L. (2001). A size-segregated particle dry deposition scheme for an atmospheric aerosol module. *Atmospheric Environment*, *35*(3), 549–560. https://doi.org/10.1016/S1352-2310(00)00326-5

Zheng, J., Zhang, Z., DeSouza-Machado, S., Ryder, C. L., Garnier, A., Di Biagio, C., et al. (2024). Assessment of dust size retrievals based on AERONET: A case study of radiative closure from visible-near-infrared to thermal infrared. *Geophysical Research Letters*, *51*(4), e2023GL106808. https://doi.org/10.1029/2023GL106808

Zheng, J., Zhang, Z., Garnier, A., Yu, H., Song, Q., Wang, C., et al. (2022). The thermal infrared optical depth of mineral dust retrieved from integrated CALIOP and IIR observations. *Remote Sensing of Environment*, *270*, 112841. https://doi.org/10.1016/j.rse.2021.112841

References From the Supporting Information

Dai, Y., Shangguan, W., Wei, N., Xin, Q., Yuan, H., Zhang, S., et al. (2019). A review of the global soil property maps for Earth system models. *SOIL*, *5*(2), 137–158. https://doi.org/10.5194/soil-5-137-2019

Hengl, T., De Jesus, J. M., Heuvelink, G. B. M., Gonzalez, M. R., Kilibarda, M., Blagotić, A., et al. (2017). SoilGrids250m: Global gridded soil information based on machine learning. *PLoS One*, *12*(2). https://doi.org/10.1371/journal.pone.0169748

King, J., Nickling, W. G., & Gillies, J. A. (2005). Representation of vegetation and other nonerodible elements in aeolian shear stress partitioning models for predicting transport threshold. *Journal of Geophysical Research*, *110*(4). https://doi.org/10.1029/2004JF000281

Nikuradse, J. (1950). Laws of flow in rough pipes (No. NACA-TM-1292). Retrieved from https://ntrs.nasa.gov/citations/19930093938

Panofsky, H. A., Tennekes, H., Lenschow, D. H., & Wyngaard, J. C. (1977). The characteristics of turbulent velocity components in the surface layer under convective conditions. *Boundary-Layer Meteorology*, *11*(3), 355–361. https://doi.org/10.1007/BF02186086

Perlwitz, J., Perez, C., & Miller, R. (2015). Predicting the mineral compositino of dust aerosols—Part 2: Model evaluation and identification of key processes with observations. *Atmospheric Chemistry and Physics Discussions*, *15*, 11629–12015.

Pierre, C., Bergametti, G., Marticorena, B., AbdourhamaneTouré, A., Rajot, J. L., & Kergoat, L. (2014). Modeling wind erosion flux and its seasonality from a cultivated sahelian surface: A case study in Niger. *Catena*, *122*, 61–71. https://doi.org/10.1016/j.catena.2014.06.006

Sherman, D. J. (1992). An equilibrium relationship for shear velocity and apparent roughness length in aeolian saltation. *Geomorphology*, *5*(3–5), 419–431. https://doi.org/10.1016/0169-555X(92)90016-H